MASTERARBEIT

Image-Guided Radiotherapy of Prostate Cancer: Organ and Patient Movement Analysis

ausgeführt am

Atominstitut

der Technischen Universität Wien

unter der Anleitung von

Ao. Univ.-Prof. DI Dr.techn. Dietmar Georg

und

Ass.-Prof. DI Markus Stock, PhD

durch

Elisabeth Steiner, BSc

An den langen Lüssen 15/8/7

1190 Wien

Wien, am 23. August 2011

Erklärung

Hiermit erkläre ich, dass ich die vorliegende Arbeit selbstständig und ohne fremde Hilfe verfasst, keine anderen als die angegebenen Quellen und Hilfsmittel benutzt und die aus anderen Quellen entnommenen Stellen als solche gekennzeichnet habe.

Wien, am 23. August 2011

Elisabeth Steiner, BSc

Acknowledgments

This thesis provides me not only with the opportunity to document the interesting work in which I have been involved for the last year, but also to thank all those who have contributed to my work, whether directly or indirectly. Please allow me a few lines to express my sincere gratitude.

First, I would like to thank Prof. Dietmar Georg for providing me the chance to perform research I totally enjoyed in two projects in the Department of Radiotherapy at the Medical University of Vienna/AKH. Also, I am deeply grateful to him for advising and supporting this thesis and guiding me through my research at so many points. In addition, I am indebted to Prof. Richard Pötter, head of the Department of Radiotherapy, for the opportunity to perform scientific work in his department.

I want to thank Markus Stock for his helpful advice in so many areas, taking the time for many fruitful discussions and giving me thought-provoking insights concerning the evaluation and interpretation of the data. Additionally, I am much indebted to him for reviewing this thesis.

I also wish to express my appreciation to Prof. Gregor Goldner for sharing his expertise in medical issues.

I owe my officemates, Barbara Knäusl and Julia Ströbele, a debt of gratitude for welcoming me as a colleague and a friend, letting me benefit from their experience, helping me in professional issues and cheering me on in stressful times.

I also would like to thank the RTTs from Linac E for sharing with me the limited space at Linac E for many hours and their knowledge concerning clinical routine, even if my questions were occasionally off-topic .

I am grateful to Åsa Palm for all the interesting conversations during the time when I conducted my project thesis at the Medical University of Vienna/AKH. These discussions piqued my curiosity and gave rise to the decision to choose a radiotherapy topic for my Master's thesis.

I am also grateful to Jasmin Tröstl for spending so much time sitting next to me in lectures or exercises and, of course, for countless homework sessions at the Mensa or the Lernraum.

Special thanks go to my wonderful family. My mum and my dad have always believed in me and supported me mentally as well as financially with unwavering devotion. I thank them for all their efforts across the last 25 years and for loving me unconditionally. Also, I would like to thank

my sister Daniela for encouraging me, giving me the feeling that I am able to master things, being a person in whom I could always trust, teaching me responsibility, and for sometimes being quite a challenge. Finally, I must express my deep gratitude to my grandparents and the rest of the family, who never miss a chance to let me know that I can always count on them.

Last but not least, I want to thank my best friend Carmen Toth for so many memorable hours, for understanding me even without using words, and for the knowledge that I can call her any time I need encouragement.

Abbreviations

3D	Three dimensional
3D-CTR	Three dimensional conformal radiotherapy
AKH	Allgemeines Krankenhaus der Stadt Wien
BMI	Body mass index
CBCT	Cone beam CT
CT	Computed tomography
CTV	Clinical target volume
DNA	Deoxyribonucleic acid
EPID	Electronic portal imaging device
ERB	Endorectal balloon
GS	Gleason score
GTV	Gross tumor volume
Gy	Gray
ICRU	International Commission on Radiation Units and Measurements
IGRT	Image-guided radiotherapy
IMRT	Intensity modulated radiotherapy
IR	Infrared
Lat	Lateral (sinister-dexter)
Linac	Linear accelerator
Long	Longitudinal (cranial-caudal)
kV	Kilovoltage
MeV	Megaelectron Volt
MLC	Multileaf collimator

MR	Magnetic resonance
MRI	Magnetic resonance imaging
MU	Monitor unit
MV	Megavoltage
OAR	Organ at risk
PLN	Pelvic lymph nodes
PRV	Planning organ at risk volume
PSA	Prostate-specific antigen
PTV	Planning target volume
SD	Standard deviation
SV	Seminal vesicles
Vert	Vertical (anterior-posterior)
VMAT	Volumetric modulated arc therapy

Contents

1 Motivation and Objectives

A crucial factor for a successful treatment utilizing radiation therapy is the accurate positioning of the patient and the target volume to apply a sufficient dose to the clinical target volume (CTV) while sparing surrounding organs at risk (OARs). When utilizing advanced treatment techniques to improve treatment outcome, like Intensity Modulated Radiotherapy (IMRT), which uses highly conformal dose distributions according to anatomical sites, a precise irradiation of the CTV is even more important. This work was focusing on radiation therapy of prostate cancer - the most frequent cancer in men, where proximate OARs are the rectal wall and the bladder wall.

Markers on the skin of the patient are normally used for setup in radiotherapy, but aligning the patient only depending on them causes gross uncertainties in case of prostate irradiation. One general issue is, that the skin's position is not fixed relative to the internal anatomy. Especially for obese patients this issue yields in a large positioning error. An image-guided setup based on bony landmarks helps to tackle this issue, but for prostate cancer irradiation this is still inaccurate because the position of the target volume is strongly dependent on the filling of the rectum and the bladder, which can not be assumed to be similar for every fraction.

Considering these challenges, at the Medical University of Vienna/AKH an image-guided treatment is performed, where the patient is aligned before treatment delivery according to the prostate's current position, obtained through three fiducial gold markers placed in the prostate. Additionally an endorectal balloon is utilized in every fraction to stabilize the position of the prostate and spare the anorectal wall.

However, even with an image-guided setup based on the position of the target volume geometrical uncertainties remain for treatment: a small setup uncertainty (in terms of the positioning uncertainty of the equipment itself and a possible clinically applied tolerance for setup) and the organ and patient movement during the fraction. These uncertainties are taken into account when adding margins to the CTV to guarantee that the CTV receives sufficient dose for eradicating cancer. However, the margins may limit the dose to the tumor region because of OARs, which may be located in or close by the PTV.

The purpose of this work, therefore, is to evaluate the intrafraction prostate and patient motion and the resulting positioning uncertainties, which occur within IMRT treatment fractions at the Medical University of Vienna/AKH, as a function of treatment time, aiming in a

possible reduction of the margins for treatment. If the positioning errors increase dramatically with progressing treatment time, a repositioning or tracking of the patient during a fraction or a reduction of treatment time should be considered. As the reproducibility of the endorectal balloon's position and its ability for prostate immobilization are arguable, a qualitative assessment of the balloons position with respect to bony anatomy and a comparison with values for margins from literature, where no daily endorectal balloon was applied, needs to be included in such a study.

2 Introduction

2.1 Basics of Radiation Oncology

Only one year after Wilhelm Conrad Röntgen discovered X-rays in November 1895 the first clinical use of fractionated radiotherapy by Leopold Freund in Vienna is documented. He successfully removed a hairy nevus covering the whole back of a 5-year-old girl [1] after reading that X-ray exposure may induce hair loss and reddened skin, but on her back a radiation ulcer remained as a result of the lack of knowledge concerning the appropriate dose. This can be seen as the foundation of radiotherapy and already shows the tightrope walk, which still has to be made nowadays when treating cancer: sufficient action for eradicating cancer on one hand, and a minimization of side effects on the other hand. The field of radiation oncology evolved rapidly since then and offers now three options of treatment: external beam radiotherapy, brachytherapy and radionuclide therapy. In **external beam radiotherapy**, which is also known as teletherapy, the radiation is applied to the patient through penetration of the skin by an external radiation source, like a linear accelerator (further explained in 2.1.3) or a Cobalt-60 teletherapy unit. Besides the most commonly used photon radiation also electrons are utilized in external beam radiotherapy to treat tumors on the or close to the surface of the patient. In **brachytherapy** one or more (sealed) radiation sources are placed near or directly within the volume, which has to be irradiated. In terms of location of the radiation sources distinction is made between surface (placement on skin), intracavitary (within natural or artificial cavities within the body), intravascular (within blood vessels) and interstitial (within the tumor itself) brachytherapy. In **radionuclide therapy**, which is strictly speaking a part of nuclear medicine, radioactive substances are administered, which have the property to concentrate in certain organs or regions of the body [2].

2.1.1 Radiation Qualities and Interactions

To assure biological effects necessary for eradicating cancer (see 2.1.2) in radiation oncology ionizing radiation, which is able to remove electrons from atoms and thus create ions, is utilized. Distinction is made between directly ionizing radiation (collision ionization through charged particles like electrons, protons, α-particles or heavy ions) and indirectly ionizing radiation (uncharged photons or neutrons). In external beam radiotherapy photon radiation and in brachytherapy γ-radiation is mainly used, so the interactions of photons inside the human

body will be discussed in detail. The energy of photons used for medical purposes in diagnostics and therapy ranges from 10 keV to 50 MeV and is produced by X-ray tubes or linear accelerators or emitted as γ-radiation from atomic nuclei (Cobalt-60 teletherapy unit). X-rays and γ-rays are photons within the same energy range and therefore physically identical, although they originate from extranuclear and intranuclear processes, respectively. When interacting with matter the energy of the uncharged photons is partly or totally absorbed or the photons are scattered (change of direction). These processes create charged secondary particles like electrons or positrons, which have the ability to ionize the surrounding matter. Therefore, photon radiation is counted among indirectly ionizing radiation. The primary interaction of photons with the penetrated material causes an attenuation of the original photon beam in terms of intensity, thus, a reduction of the number of photons within the beam. For a mono-energetic, narrow and parallel photon beam geometry the attenuation of intensity can be described as decreasing exponentially within a tissue of constant density and atomic number:

$$I(d) = I_0 \cdot e^{-\mu \cdot d} \tag{2.1}$$

The intensity of the incoming radiation beam is I_0, the intensity at a depth d of the material is $I(d)$ and the material and energy dependent **linear attenuation coefficient** μ is proportional to the density of the absorber material and made up of contributions regarding the physical processes involved.

$$\mu = \tau + \sigma_C + \sigma_{coh} + \kappa_{pair} + \kappa_{triplet} + \sigma_{nph} \tag{2.2}$$

Processes, where photons interact with the atomic shell of the absorber are **coherent scattering** with the coefficient σ_{coh}, the **Compton effect** (incoherent scattering) with σ_C and the **photoelectric effect** with τ. When photons interact with the Coulomb field of atomic nuclei one speaks of **pair production** with the coefficients κ_{pair} and $\kappa_{triplet}$, and of the **nuclear photoelectric effect** with σ_{nph} when photons interact with the nuclei themselves. The quantitative role of the nuclear photoelectric effect is negligible. Therefore, the coefficient σ_{nph} is often omitted. As the attenuation coefficients are proportional to the density ρ of the absorber material for practical reasons the **mass attenuation coefficient** μ/ρ is frequently used instead of the linear attenuation coefficient [2–4].

Coherent Scattering

The process of photons interacting with matter is called coherent scattering when there is no overall energy transfer to the atoms of the material and ionization does not occur. The

photon interacts with an electron of an atom in such a way that the energy of the photon is absorbed and the electrons of the atom start to vibrate at the frequency of the photon. Finally the absorbed radiation is emitted as a photon, which is of the same wavelength as of the original one (see Fig. 2.1). For human tissue implicating low atomic numbers coherent scattering is only

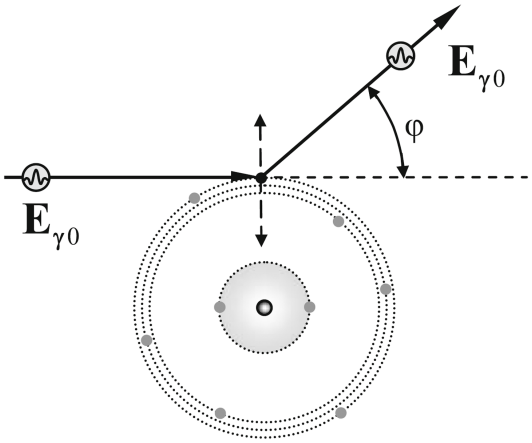

Figure 2.1: Coherent scattering (from [3], p185).

relevant up to energies of about 20 keV. Therefore, coherent scattering processes are negligible in radiotherapy [3].

Photoelectric Effect

The process where a photon carries all its energy over to an electron orbiting around an atom, which is, subsequently, able to leave the atomic shell, is called photoelectric effect (see Fig. 2.2). Therefore, the energy of the photon has to be higher than the binding energy of the electron. The kinetic energy of the electron yields to

$$E_{kin} = E_\gamma - E_b \tag{2.3}$$

which is the difference of the energy of the incoming photon and the binding energy of the orbital electron. Strictly speaking, for reason of conservation of momentum a very small part of the energy of the photon is transferred to the atom as well. This is obvious when having a look at the process in the center-of-mass-system. Before the collision the photon and the atom move towards each other with a resulting overall momentum of zero. After the collision the electron leaves the atomic shell with the main component of the momentum and therefore the remaining atom has to get a recoil momentum. As the nucleus is much heavier than the leaving

electron, the energy ratio transferred to the atom is negligible. The hole in the shell created by the leaving electron can now be filled with an electron from an outer shell by emitting the energy difference as a characteristic photon or transferring it to another electron, which is able to leave the atom as a so-called Auger electron. The probability for photoelectric interaction is

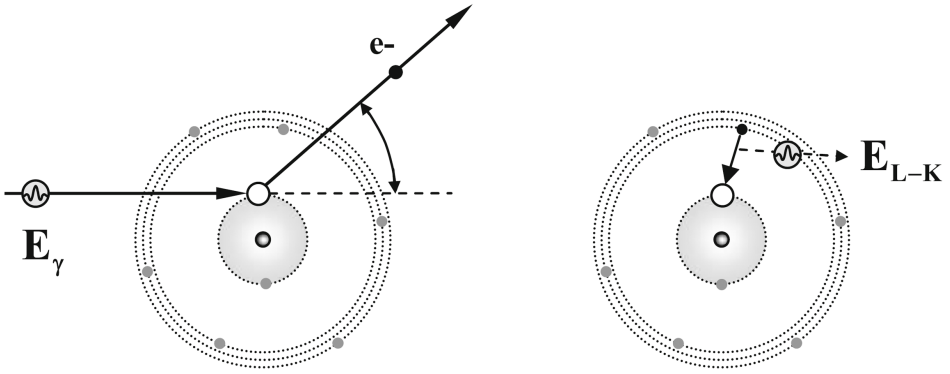

Figure 2.2: Photoelectric effect (from [3], p160).

indicated through the photoabsorption coefficient τ, which depends on the density ρ as well as on the atomic number Z of the absorber material and the photon energy E_γ. The interaction probability is strongly dependent on the atomic number of the absorber material and reaches the largest values for dense, heavy elements.

$$\tau \propto \rho \cdot Z^3 \tag{2.4}$$

The difference in X-ray absorption for materials with different atomic numbers stated in equation 2.4 establishes the basis of diagnostic radiology. For radiation protection in diagnostic X-ray imaging, hence, high Z materials are utilized as well. The probability of photoelectric absorption decreases with increasing photon energy like

$$\tau \propto \rho \cdot \frac{1}{E_\gamma^3} \tag{2.5}$$

except for discontinuities called absorption edges, when the energy reaches the binding energy of the next inner shell and the probability of interaction gets much higher (see Fig. 2.3).

The combination of equations 2.4 and 2.5 gives

$$\tau \propto \rho \cdot \frac{Z^3}{E_\gamma^3} \tag{2.6}$$

for the photoabsorption coefficient. The angular distribution of the ejected electrons relative to the direction of the incident photons depends on the photon energy. For lower energies of the

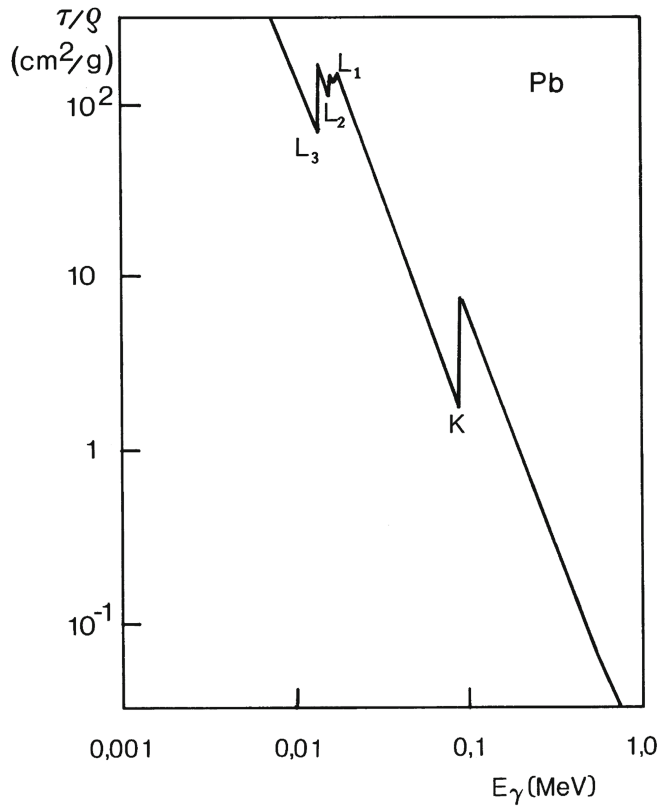

Figure 2.3: Energy dependence of the mass-photoabsorption coefficient τ/ρ for lead with the absorption edges L_1-L_3 and K (from [3], p162).

photons the electrons are emitted almost perpendicular to the original photon beam. The higher the energies of the photons get, the more the electrons are emitted in forward direction [3, 5].

Compton Effect

The Compton effect describes the incoherent interaction of a photon with an outer, weak-bonded shell electron of the absorber material. Hence the binding energy of the electron is much less than the energy of the interacting photon and the photon transfers parts of its energy and momentum to the electron. The electron is able to leave the atomic shell at an angle θ relative to the direction of the incident photon and the photon gets scattered at an angle φ from its original path (see Fig. 2.4). The probability for the occurrence of the Compton effect is described through the Compton attenuation coefficient

$$\sigma_C = \sigma_{sc} + \sigma_{tr} \tag{2.7}$$

made up of the Compton scatter coefficient σ_{sc} for the incoherent photon scattering and the Compton energy transfer coefficient σ_{tr} for the energy transfer to the Compton electron. Due to the fact that the Compton effect involves an outer electron, the field of the nucleus is shielded significantly by the inner electrons. Therefore, the Compton attenuation coefficient is independent of the atomic number of the absorber material. An empirical, gross approximation for energy dependence the Compton attenuation coefficient, which is proportional to the density ρ of the absorber material, is given by

$$\sigma_C \propto \rho \cdot \frac{1}{E_\gamma^n} \tag{2.8}$$

whereas E_γ is the energy of the incident photon and n ranges from 0.5 to 1. When describing

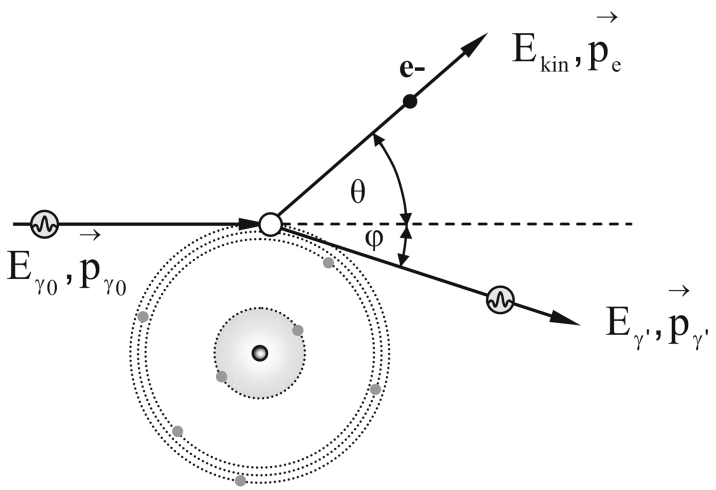

Figure 2.4: Compton effect (from [3], p165).

the process as an elastic collision between two particles with the electron being at rest before the collision, energy and momentum conservation laws provide the relation

$$E'_\gamma = \frac{E_\gamma}{1 + \frac{E_\gamma}{m_0 c^2} \cdot (1 - \cos\varphi)} \tag{2.9}$$

between the energy E_γ of the incident photon, the energy of the scattered photon E'_γ, the rest energy $m_0 c^2$ of the electron and the photon's scattering angle φ. Both Compton electrons and scattered photons show angle and energy distributions depending on the energy of the primary photons. The frequency of occurrence for certain scattering angles at certain photon energies can be calculated by applying relativistic quantum theory. For photon energies, which are much lower than the rest energy of the electrons (511 keV), the energy of the scattered photon is almost equal to the energy of the incident photon and to a large extent independent of the

scattering angle. Therefore, for soft X-rays used in diagnostic imaging one has to be aware of this fact concerning radiation protection. The energy transfer to the Compton electrons hence is low, so their range is limited and no dose accumulation effect occurs. However, for photon energies exceeding the rest energy of the electron ($E_\gamma >> 511keV$) the energy-relation term in the denominator in equation 2.9 gets (considerably) larger than 1 and accordingly the energy transfer to the Compton electron is larger than for low-energy photon radiation and more dependent on the scattering angle. The Compton electrons thus have a larger operating distance, in materials with low atomic numbers as water or human tissue up to a few centimeters. This leads to the dose accumulation effect on material boundaries [3, 5].

Pair Production

If the photon energy exceeds $2 \cdot 511$ keV, whereat 511 keV is the rest mass of an electron, the process of pair production may occur in the electromagnetic field of the nucleus. A pair of a negatively charged electron and a positively charged positron is created from the photon, which is totally absorbed in this process. The energy of the incident photon is converted into the rest masses of the electron and the positron and their kinetic energies, whereat the total available kinetic energy is:

$$E_{kin} = E_\gamma - 2 \cdot m_0 c^2 = E_\gamma - 1022keV \tag{2.10}$$

The nucleus itself keeps unchanged, its presence is only necessary for energy and momentum conservation reasons while creating the electron-positron pair. The probability for pair production increases with the logarithm of the photon energy. It is also proportional to the density of the absorber material and to the relation Z^2/A, which is approximately Z for light and moderately heavy elements. For pair production in the field of an atomic nucleus hence the relation

$$\kappa_{pair} \propto Z \cdot \rho \cdot \log E_\gamma \tag{2.11}$$

for photon energies $E_\gamma > 1022$ keV is valid. The electron and the positron propagate through the absorber material and deposit their kinetic energy in multiple collisions in matter. When the positron gets at rest in the vicinity of a shell electron, it recombines with the electron by producing two photons of the so-called **annihilation radiation**. In this process the rest mass of the two particles is transformed into two photons, each with an energy of 511 keV, which move in opposite directions due to conservation of momentum. If the positron is not totally at rest when annihilating, the remaining kinetic energy will also be transformed into energy of the created photons. The annihilation photons can be absorbed through photoelectric or Compton

processes, but usually leave finite absorbers without interaction. Therefore, they contribute only to some extent to the energy dose within the absorber. At very high photon energies and atomic numbers pair production gets the dominating interaction of photons and matter [3, 5].

Pair production takes rarely place in the field of a shell electron. The shell electron, whose mass is three orders of magnitude smaller than the mass of the nucleus, is leaving the atom in this process. It propagates through the absorber material alongside with the pair of electron and positron and all deposit their energy in multiple collisions within the absorber. Because of the three involved particles this process is called **triplet production** and its probability is described through the coefficient $\kappa_{triplet}$. For energy and momentum conservation reasons triplet production gets possible at photon energies $E_\gamma > 4 \cdot 511$ keV [3].

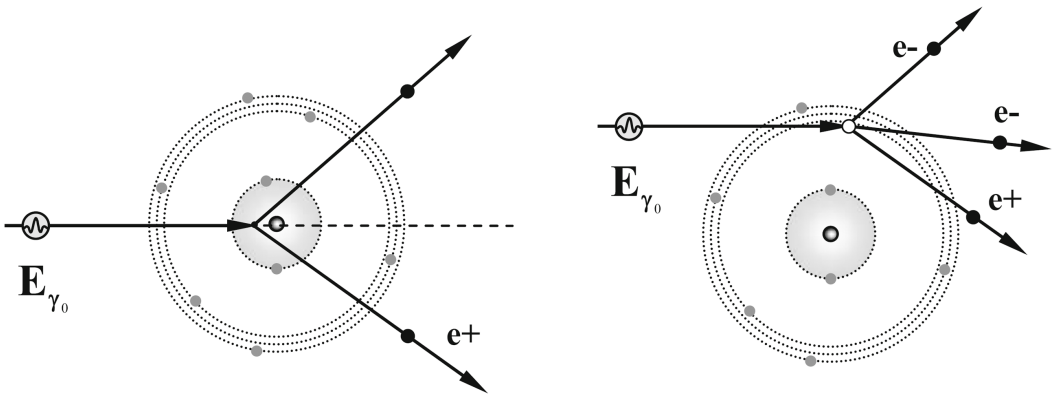

Figure 2.5: Pair production processes: left side: pair production in the Coulomb field of an atomic nucleus; right side: triplet production in the Coulomb field of a shell electron (from [3], p182).

Relative Importance of Interactions

As seen in equation 2.2 at the begin of section 2.1.1 the linear attenuation coefficient is made up of the coefficients, which state the probability for the specific interactions of photons in matter. All the contributions depend on the energy of the incident photon radiation and/or the atomic number of the absorber material. Hence Fig. 2.6 gives and overview of the relative importance of certain processes at different energies and atomic numbers.

The photoelectric effect dominates for heavy elements and photon energies up to 1 MeV. Radiation protection materials like lead, tungsten and uranium work in this energy range via the photoelectric effect, avoiding the creation of scattered radiation. However, the creation of

characteristic X-rays in heavy materials has to be considered. In human tissue the photoelectric effect contributes only at low photon energies, for example in diagnostic imaging, noticeable to the overall energy transfer.

The Compton effect dominates a wide range of photon energies and for low atomic numbers up to Z = 10. Therefore, it is the most important process in radiotherapy, keeping in mind that human tissue is of Z ≈ 7. Within the energy range of 1-4 MeV, which is dominated by the Compton effect independently of the atomic number, the mass attenuation coefficients are independent of the material and for all atomic numbers almost equal.

Coherent scattering is negligible for energies exceeding 20 keV when compared to the other interaction processes. In particular, due to lacking energy transfer in this process it does not contribute to the generation of an energy dose within the absorber.

Pair production takes place at photon energies larger than 1.022 MeV and gets some importance for low atomic number starting with energies of about 10-20 MeV. For heavy elements (Z > 20) pair production is the dominating process for photon energies larger than 10 MeV [3].

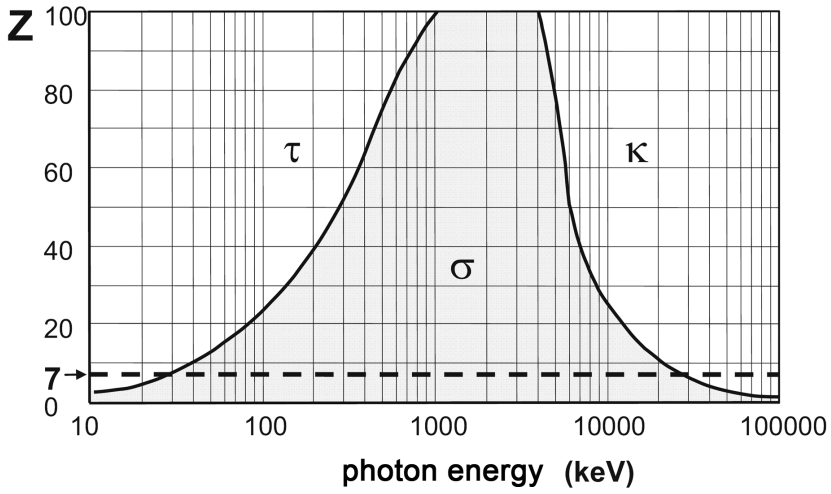

Figure 2.6: Main relative interaction processes depending on photon energy and atomic number of absorber. The dashed line at an atomic number of Z = 7 for human tissue emphasizes the area involved in radiotherapy (from [3], p193).

2.1.2 Radiation Biology

When irradiating human tissue the first phase of interaction are the physical processes described in the previous section 2.1.1, which occur on a time scale of 10^{-16} s to 10^{-13} s. The

energy transfer to the tissue in these interactions leads to ionized or excited atoms. Molecules consisting of these atoms tend to fall apart, creating free radicals, which are highly unstable and transfer chemical damage to other molecules in their vicinity. Human cells are made up of biological molecules as proteins, enzymes, lipids, DNA and about 80 % water. If biomolecules are damaged directly through the radiation field, one speaks of **direct radiation effects**. Given that water is the most abundant molecule within the cell, the most free radicals originate from the radiolysis of water

$$H_2O \Longrightarrow H_2O^+ + e^- \tag{2.12}$$

$$H_2O \Longrightarrow H_2O^* \Longrightarrow^{\bullet} OH + H^{\bullet} \tag{2.13}$$

where the process in the upper equation 2.12 states an ionization and the process in the lower equation 2.13 an excitation and subsequent fission of a water molecule. If free oxygen is present within a cell, additional free radicals are produced

$$H^{\bullet} + O_2 \Longrightarrow HO_2^{\bullet} \tag{2.14}$$

$$e^- + O_2 + H^+ \Longrightarrow HO_2^{\bullet} \tag{2.15}$$

$$2HO_2^{\bullet} \Longrightarrow H_2O_2 + O_2 \tag{2.16}$$

and increase the cell's radiosensitivity.

The **oxygen enhancement ratio** states the ratio of the radiation dose in hypoxia to the radiation dose in air, leading to the same biological effect. A fact that has to be considered in treatment planning therefore is that solid tumors tend to have an oxygen-deprived center due to insufficient blood supply, which is less sensitive to radiation.

One speaks of **indirect radiation effects** when the free radicals generate damage in molecules in their proximity in the chemical phase. This is not critical for the cell's viability when a few molecules of a highly abundant type are destroyed. However, if the DNA gets attacked, it may lose some specific functions through modification or loss of genes, which are crucial for survival of the cell. Damages of the DNA can be single-strand breaks, double-strand breaks or a loss or modification of bases, which group to genes. Strand breaks can be fixed, although the probability for double-strand breaks to be repaired is much smaller than for single-strand breaks. A dose of 1 Gy causes about $2 \cdot 10^5$ ionizations in a cell, which induce about 1000 single-strand breaks and approximately 40 double-strand breaks. Nevertheless due to efficient repair processes most cells survive. These processes, where free radicals interact with molecules, occur on time scales of about 10^{-3} s.

The third phase called biological phase happens on time scales from 10^{-2} s to some years or even decades and implicates changes in cell metabolism, cell death, gene material mutation and malignant degeneration of cells.

The key of a successful cancer treatment is selectivity - killing tumor cells while not over-radiating normal structures. Therefore, the delivery of high dose has to be limited to a possibly small volume including the tumor. A simplified illustration of the idea for a successful treatment can be seen in Fig. 2.7, however, prescribing the dose of the peak of the dashed curve is not clinical practice, as the damage to normal tissue might reach unacceptable extents. Also,

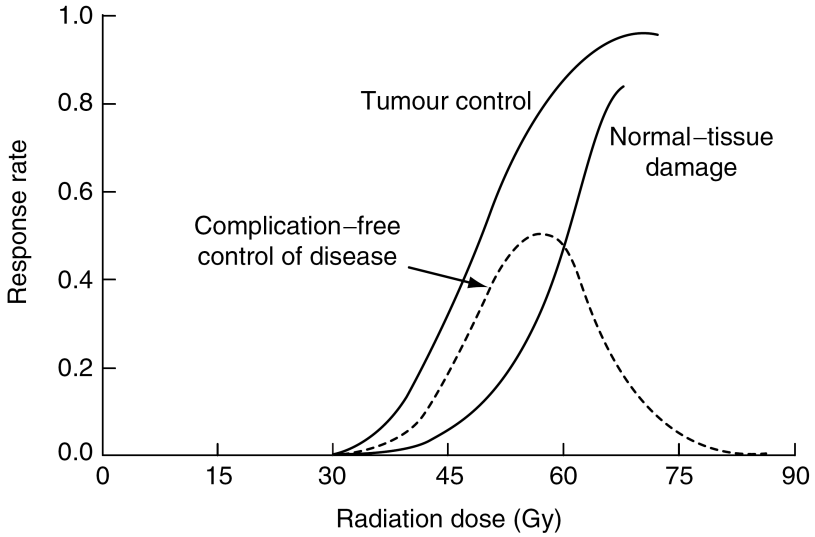

Figure 2.7: Probability of tumor control and normal-tissue damage as a function of radiation dose resulting in complication-free tumor control (from [6], p154).

the applied dose in external beam radiotherapy is split into daily fractions to allow the repair mechanisms of the cells to work, although the necessary total dose to the tumor increases with the number of fractions. This **fractionation** works because normal structures have a larger ability to recover than most tumors. Fractionation can be optimized by use of the linear-quadratic approach, which accounts for normal tissues and tumors showing a difference in response to a change in dose fractionation [3, 6, 7].

2.1.3 Linear Accelerator

For creation of megavoltage (MV) beams used in radiotherapy linear accelerators are most commonly utilized. In contrast to kV beams, MV beams provide a much higher penetration depth, which offers the possibility to treat deeply situated tumors and additionally the advantage

of skin sparing through dose build-up effect.

High-energy photon beams produced by a linear accelerator show an energy spectrum comparable to kV X-ray beams. The mean energy of the beam can be obtained by applying a thumb rule and dividing the nominal energy of the beam by 3. Hence a nominal 6 MV beam has a mean energy of about 2 MeV. The energy, which can be achieved with linacs, is limited through space constraints to values of about 22 MeV, but is sufficient for treating tumors inside the human body.

A linear accelerator consists of five main components: the energy supply, the modulator, the accelerating device, the treatment head and the control unit (see Fig. 2.8). In the mod-

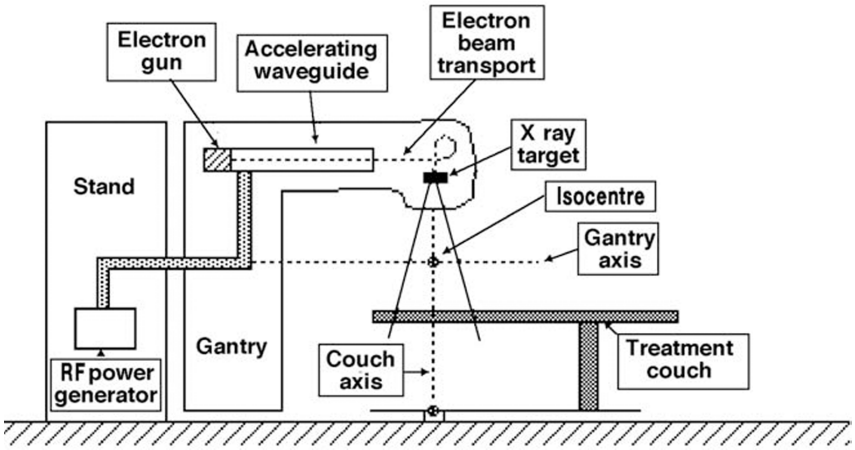

Figure 2.8: Typical design of a linear accelerator (from [8], p140).

ulator high-voltage pulses are created, which supply the microwave source and the electron gun. Electrons destined to be accelerated are created in the electron gun from a heated cathode in thermionic emission. The microwave power source, which can be a magnetron or a klystron, creates powerful radiofrequency waves that accelerate the electrons in the accelerating waveguide with the radiofrequency power source determining the maximum energy of the accelerator. There are two types of accelerating waveguides depending on the manufacturer: travelling waveguides (Elekta), where the wave is propagated along the axis of the guide; and standing waveguides (Varian, Mitsubishi, Siemens), where the wave is stationary. In both of them the electron bunches, which are accelerated, have to be steered and focused because of their tendency to diverge caused by repulsive coulomb forces between the electrons and radial components of the accelerating field. The most obvious setup would be mounting the tube for acceleration parallel to the central axis of radiation beam, but for the required high energies

(> 6 MV) of the electrons this turns out to be impractical in terms of space. Hence the accelerating waveguide is mounted perpendicular to the radiation beam and a bending of the beam of about 90° is necessary. As a 90° dipole bending magnet causes a beam divergence as a result of energy spread, lateral displacement and beam divergence at the entrance (see Fig. 2.9), 270° bending magnets are utilized.

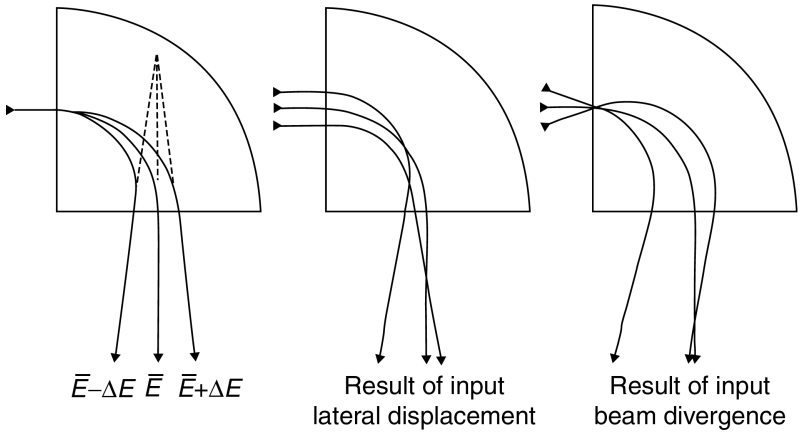

Figure 2.9: Simple 90°bending magnet (from [6], p212).

The treatment head of the linear accelerator consists of elements for production, shaping and monitoring the photon or electron treatment beam (see Fig. 2.10). Mostly treatment is performed with photon beams. In order to generate an MV photon beam out of the electron beam, the electrons hit a (retractable) high atomic number metal target (usually tungsten) emitting bremsstrahlung as they are decelerated. At MV beam energies bremsstrahlung is mainly emitted in forward direction, hence the target acts as a transmission target. To obtain a homogenous beam profile a flattening filter is used (see Fig. 2.11). However, nowadays there is a tendency to remove the flattening filter out of the beam for an increased dose rate and reduced scatter and leakage radiation [9]. Additionally, a circular primary collimator close to the source and an adjustable secondary collimator, which is capable to create a square or rectangular field, are included in the treatment head. The secondary collimator is organized in four blocks, a pair of them forming the upper and the lower jaws, respectively. An optional multileaf collimator (MLC) consists of up to 80 pairs of leaves that can move independently and provides the option to shape the field individually (see Fig. 2.10). Transmission ionization chambers are used for steering of the beam and for dose monitoring and guarantee that the beam output fulfills the requirements [2, 6, 8].

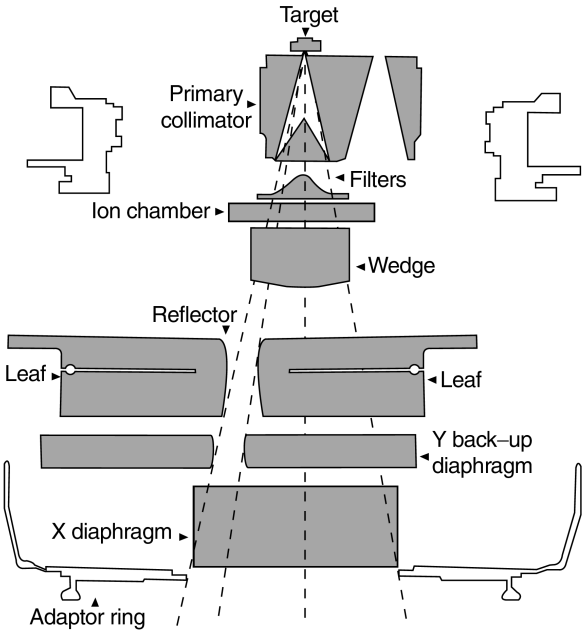

Figure 2.10: Diagram of an Elekta treatment head including a multileaf collimator (from [6], p221).

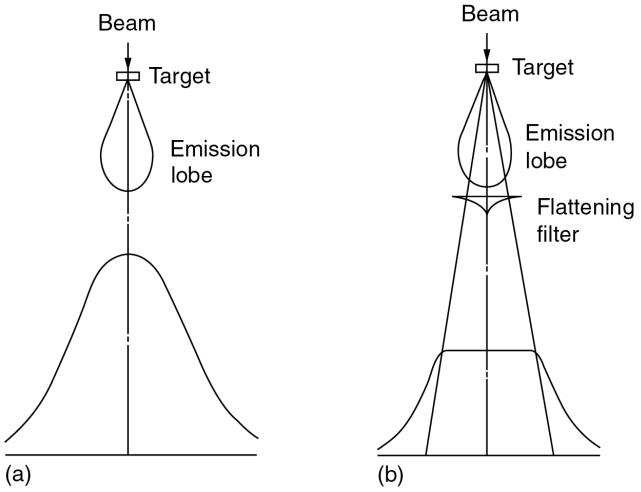

Figure 2.11: Comparison of a beam a) with and b) without a flattening filter (from [6], p216).

2.1.4 Imaging in Radiation Oncology

Imaging is employed in state-of-the-art radiation oncology throughout the whole radiotherapy chain, starting with diagnosis, staging, treatment planning and finally execution. The implementation of computed tomography imaging in radiation oncology caused a large progress

in terms of knowledge concerning the target volume and normal tissue structures. Consequently, three dimensional dose calculations and the conformation of individually shaped target volumes for patients were enabled. Planning became more complex, but the higher efforts are justified through enhanced patient outcomes, for example in terms of quality of life or curative rates. However, an adequate education and common guidelines for tumor and normal tissue definition are crucial. Functional imaging supplying information concerning biological, metabolic or physiological processes may offer the knowledge for additional improvement of radiation delivery. For treatment execution the integration of various imaging modalities in the treatment room assures the accurate delivery of a treatment plan [10], for more details related to image-guided radiotherapy see section 2.3.2.

2.2 Volume Concepts in Radiotherapy

An important step for a successful treatment is the definition and delineation of volumes, which are treated to a prescribed dose, as a common language for all professional groups involved in radiotherapy. Introduced in ICRU Reports 50, 62, 71 and finally especially for IMRT treatments in ICRU Report 83 the following volume concepts provide the basis for planning and treatment (see Fig. 2.12).

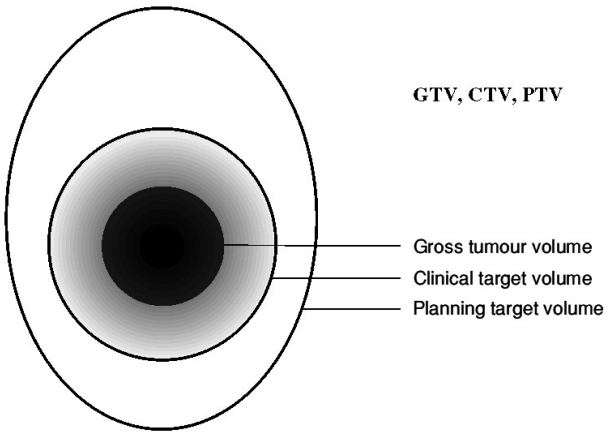

Figure 2.12: Volumes for planning in radiotherapy according to ICRU Report 50 (from [11]).

GTV

According to ICRU Report 50 *the gross tumor volume (GTV) is the gross palpable or visible/demonstrable extent and location of malignant growth.* Therefore, the GTV may consist of the primary tumor, metastatic regional node(s), or distant metastasis. For the primary tumor

and regional node(s) different GTVs are defined normally, except for cases where there can not be distinguished between both of them. Different diagnostic methods are used to determine the shape, size and location of the GTV. Clinical examination (inspection, palpation, endoscopy, ...) and several imaging techniques (X-ray, CT, ultrasound, MRI, ...) provide the information needed to delineate the GTV. Depending on the imaging modalities, which are the basis of the GTV delineation, the GTV might appear different in size and shape. For precision radiotherapy, CT and MR scans are the most common techniques to define the GTV. Additionally, positron emission tomography (PET) or functional MRI are used for contouring and for follow-up examinations. Also, they may provide information about some key biological factors that may have impact on the treatment outcome, which is a subject of recent and future clinical studies. No GTV can be defined in case of complete surgical resection [12, 13].

CTV

Outside the GTV there might be tissues that bear risk for microscopic infiltration, which can not be detected through clinical examination. These tissues have to be irradiated with sufficient dose also, which leads to an increase of the volume treated to a dose prescription from the GTV to the clinical target volume (CTV). The CTV, as defined in ICRU Report 50: *The clinical target volume is a tissue volume that contains a demonstrable GTV and/or subclinical microscopic malignant disease, which has to be eliminated. This volume thus has to be treated adequately in order to achieve the aim of therapy, cure or palliation.* The CTV is delineated based on clinical experience, concerning the probabilities for microscopic dissemination according to oncologic and biological factors [12, 13].

PTV

Due to uncertainties in patient setup for treatment, internal organ- and therefore CTV-motion, variations in shape and size of the CTV and/or variations in beam geometry an irradiation of the whole CTV to the prescribed dose is not possible. Taking these aspects into account leads to the definition of the planning target volume (PTV) in ICRU Report 50: *The planning target volume is a geometrical concept, and it is defined to select appropriate beam sizes and beam arrangements, taking into consideration the net effect of all the possible geometrical variations, in order to ensure that the prescribed dose is actually absorbed in the CTV.* The PTV is stated in relation to a fixed coordinate system as skin marks, bony landmarks or internal markers. The margin surrounding the CTV that creates the PTV depends on the magnitude

of the variations in setup and organ motion and may surpass anatomical borders. For prostate cancer irradiation the CTV-to-PTV margin is often 1 cm, but less in anterior-posterior direction to spare the rectum. Image-guidance can significantly reduce the required margins [12, 13].

OAR

According to ICRU Report 50 *Organs at risk (OARs) are normal tissues whose radiation sensitivity may significantly influence treatment planning and/or prescribed dose.* In general all non-target tissues could be OARs, but usually normal tissues are considered as OARs depending on their location in relation to the CTV. In terms of functionality OARs are divided into "serial", "parallel" and "serial-parallel" structures. Serial organs like the spinal cord consist of a chain of units and if only one of them gets destroyed, it is fatal, because all nerve functions downstream of that point are affected. Parallel structures like the lung, however, consist of independently working functional units and the organ will still work when a limited number of them gets destroyed. The kidney, for example, is an organ which is a combination of both serial and parallel structures. Hence the properties of proximate OARs create dose-volume constraints for irradiation, which were mostly obtained from retrospective clinical observations of normal tissue complications [12, 13].

PRV

When defining the OAR volumes uncertainties through setup and organ movement have to be considered in the same way as for the CTV. Along the lines of creating the PTV now a volume called planning organ at risk volume (PRV) is defined. Depending on whether the OAR is of serial or of parallel structure the margin around the OAR is more or less relevant. The possible overlap of PTV and PRV leads to the application of priority rules and a separation of the PTV into sub-PTVs with certain dose constraints in the planning process [12, 13].

2.3 Advanced Treatment Techniques

Conventional radiotherapy uses simple rectangular treatment fields which are not sufficient to provide an ideal irradiation according to irregular-shaped tumor volumes. Accordingly, normal tissue has to be irradiated as well to guarantee that the CTV receives the prescribed dose. Also, one has to be aware of setup and motion uncertainties which might influence the dose delivery. With the aim to deliver a possibly high dose to the tumor while sparring the surrounding normal tissue and organs at risk new approaches for the delivery of radiotherapy have been developed. Improvements have been made by using in-room imaging devices and advanced treat-

ment techniques as three dimensional conformal radiotherapy (3D-CRT), intensity modulated radiotherapy (IMRT) and volumetric modulated arc therapy (VMAT) [14, 15].

As this work investigates the intrafraction organ and patient movement for patients who receive IMRT treatments, IMRT and image-guided radiotherapy (IGRT) will be discussed in more detail.

2.3.1 IMRT

Intensity modulated radiotherapy is a technique which offers an enhancement of conformal irradiation according to three dimensional treatment planning. IMRT uses treatment fields with nonuniform photon fluence. This can be achieved by dividing one field into many little subfields of uniform photon fluence, which can be varied independently. Hence the dose to the tumor from one direction can be reduced when there is an organ at risk within the treatment field and the missing dose can be compensated from another direction. Therefore, IMRT deals well with irregularly-shaped tumors and is able to create concavities in treatment volumes. One IMRT field may create an inhomogeneous dose distribution in the CTV, but the superposition of treatment fields of nonuniform photon fluence from different directions finally gives an uniform dose distribution in the CTV. This approach reduces high dose areas outside the CTV and therefore supports dose escalation for the tumor (see Fig. 2.13) [7, 14].

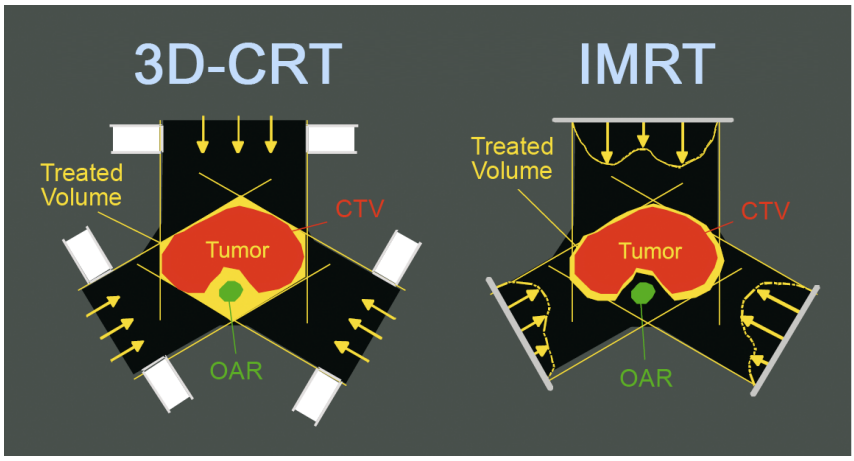

Figure 2.13: Comparison of 3D-CRT and IMRT: for IMRT treatment the OAR is spared, while the dose to the CTV is the same (adapted from [7]).

There are different approaches to implement IMRT. The nonuniform photon fluence within one field can be reached in a traditional way through using compensators within the beam. These compensators act as absorbers, which show an inverse profile to the intensity profile

and create the intensity modulation for a single field. However, this technique shows several drawbacks: compensators have to be fabricated for every single field, they have to be replaced for each field and therefore require treatment breaks and someone, who enters the treatment room every time before a new field is applied, and they cause scatter radiation, which increases the dose outside the field. Hence other techniques have been established in IMRT, which utilize computer-controlled collimator leaves to adjust the field for treatment. The so-called multileaf collimators (MLCs) are used in two different ways to vary the time of radiation exposure for a certain region to create the intensity modulation within a field: the step-and-shoot technique and the dynamic intensity modulation, also known as sliding-window technique. The step-and-shoot method is implemented at the Elekta Linac used for the study, which means that the beam is off, while the leaves of the collimator move to the next position to create and arbitrary shaped field corresponding to the treatment plan. After the field has been created the beam is turned on for a certain time calculated by the treatment planning system. Subsequently, the beam is turned off again and the leaves move to their next position. On the contrary, the field is shaped utilizing the MLC in dynamic intensity modulation while the beam is on, therefore, the technique is called sliding-window IMRT. This method is more complicated to handle, because in addition to the position, the speed of the leaves has to be monitored as well. However, dynamic intensity modulation offers the advantage of shorter treatment times [7, 16].

As mentioned in the paragraph above treatment planning is essential to master IMRT. Inverse treatment planning calculates the positions of the leaves and the beam-on times according to dose requirements in target volumes and organs at risk achieved by clinical objectives. Constraints, like the prescribed dose to the target volume, the minimum dose to the target volume and maximum dose values for various OARs defined in advance, provide the basis of an optimization task, which has to be solved during the treatment planning process. The importance of a constraint is expressed by its weighting factor. Thus the treatment planning system has to figure out an optimal agreement between dose constraints, degrees of freedom like the number of fields and limitations like the impossibility of the implementation of very steep dose gradients, with the sequencer performing the task to translate the firstly calculated intensity profile derived during optimization into a deliverable treatment [6, 7, 17].

As IMRT prolongs the treatment time significantly, it is clinically applied only, if the dose distribution can be optimized thus far, that an improvement of the treatment outcome, like an increase of long-term tumor control probability and a reduction of toxicity, can be expected [7].

2.3.2 IGRT

With the aim to reduce the target volume when irradiating tumors to spare OARs, the precise alignment of the patient/target volume became more and more important. Especially for treatments like IMRT, where sharp dose gradients occur, an accurate positioning is essential. In general, there are different approaches to implement image-guided radiotherapy (IGRT). The traditional approach is to use the megavoltage (MV) treatment beam and an electronic portal imaging device (EPID). It is also possible to use this setup as an MV cone beam CT (CBCT). However, using the treatment beam for imaging does not provide sufficient soft tissue contrast for alignment of structures like the prostate and causes additionally a high dose to the imaged area. Therefore, kilovoltage (kV) imaging modalities were placed inside the treatment room. Current kV systems are CT-on-rails - a conventional CT scanner, which is mounted on rails and can be moved to acquire scans of the patients on the treatment couch, ceiling/floor-mounted systems - so called stereoscopic imaging systems are mounted in a steady position in the treatment room and are able to provide 3D information due to the special imaging geometry, and gantry-mounted systems - are usually mounted perpendicular to the central axis of the treatment beam and can be used for planar projection images or as a cone beam CT (CBCT). In this work position verification was performed with the floor-mounted BrainLAB ExacTrac system (for further explanation see section 3.1.2). In-room imaging for patient setup decreases inter-fractional positioning errors, but still one has to face challenges when dealing with intrafraction motion like organ movement during one fraction [10, 14, 18, 19].

2.4 Margins in Radiotherapy

In highly accurate external beam radiotherapy **geometrical uncertainties** still emerge. As patient setup is performed based on markers on the skin, the motion of skin relative to internal anatomy limits the reproducibility of the setup at the planning CT and leads to a **setup error**, showing a random and a systematic component. Due to **organ motion** with respect to bony anatomy, additional uncertainties are caused. The systematic component of the organ motion error originates from the arbitrary position of the organ during the planning CT scan, the random component from the variation of the position for different fractions or during one fraction.

Hence margins are utilized to deal with errors that occur in treatment planning and execution. As already mentioned in section 2.2 the CTV is expanded with a safety margin to obtain the PTV, which is given a high dose to ensure that the CTV receives the required dose despite

Table 2.1: Determination of group systematic error, M, standard deviation of the systematic error, Σ, and standard deviation of the random error, σ, e.g. from values for a shift in one direction (from [20]).

	Patient1	Patient2	Patient3	Patient4	
Day 1	2	4	1	3	
Day 2	1	-2	-1	-3	
Day 3	1	2	2	-2	
Day 4	1	0	2	1	
Mean	1.25	1	1	-0.25	↗ Mean = M = 0.75 ↘ SD = Σ = 0.68
SD	0.50	2.58	1.41	2.75	→ RMS = σ = 2.03

the presence of **geometrical errors**, considering the fact that an increase of the target volume leads to a high-dose irradiation of normal tissue as well. Therefore, margins should be sufficient, but not excessive. Calculating margins for treatment, one has to be aware that random deviations cause a blurring of the dose distribution, while systematic deviations shift the dose distribution (see Fig. 2.14). Therefore, a systematic error is much more critical, a fact that will be accounted for in van Herk's formula for margin calculation.

Following the recipe of van Herk for margin calculation, for each patient the mean and the standard deviation of an error, e.g. a shift in one direction, for the whole treatment course are calculated. Out of the mean values for each patient the overall mean error (group systematic error), M, and the standard deviation of the systematic error, Σ, for all patients are determined. The standard deviation of the random error, σ, is obtained as the root mean square of the individual standard deviations (see Tab. 2.1 for recipe).

To assure that the minimum cumulative CTV dose is at least 95 % of the prescribed dose for 90 % of the patients van Herk's formula for the margin

$$Margin = 2.5\Sigma + 0.7\sigma \tag{2.17}$$

is applied.

The use of image guidance for patient setup helps to reduce the CTV-to-PTV margins. However, even the best image-guidance systems cannot eliminate all variations, due to the fact that they have uncertainties themselves and the deformation of the patient's anatomy cannot be eliminated.

Errors also occur as a result of **delineation uncertainties** of the GTV caused by limited resolution of imaging modalities, inter- and intraobserver variations, interpretation differences between imaging modalities and the application of different or unclear guidelines for target volume delineation. All these components lead to a systematic error in irradiation of a patient, because they influence the whole treatment series. The CTV is made up of the GTV and regions with **suspected microscopic tumor**. Due to the unknown extent of the microscopic tumor this is also a source for a systematic error [20, 21].

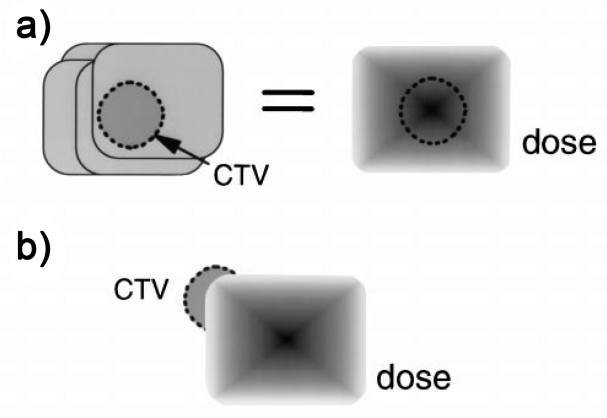

Figure 2.14: Impact of a) random and b) systematic geometrical uncertainties on the dose distribution (from [21]).

2.5 Prostate Cancer

Prostate cancer is the most frequent cancer in men with a cumulative risk of incidence from age 0-74 of 7.8 % in the more developed areas. The highest detection rates occur in developed countries because of the application of the prostate-specific antigen (PSA) testing, which enables an early detection. In comparison, the mortality rates for prostate cancer are the highest in developing countries [22].

The prostate is an approximately chestnut-sized gland located in the pelvic region, caudal of the bladder and anterior of the rectum, through which it can be palpated. For a high percentage of men a benign increase of the prostate (benign prostatic hyperplasia) emerges at higher ages, starting with an age of about 55 to 60 [23]. For prostate cancer diagnosis digital rectal examination, PSA assessment (where a PSA-level above 4 ng/ml usually leads to a subsequent biopsy), transrectal ultrasound, biopsy, CT- and MR-imaging are utilized. Prostate carcinomas are usually located in the peripheral regions of the prostate and can therefore be detected through a rectal examination.

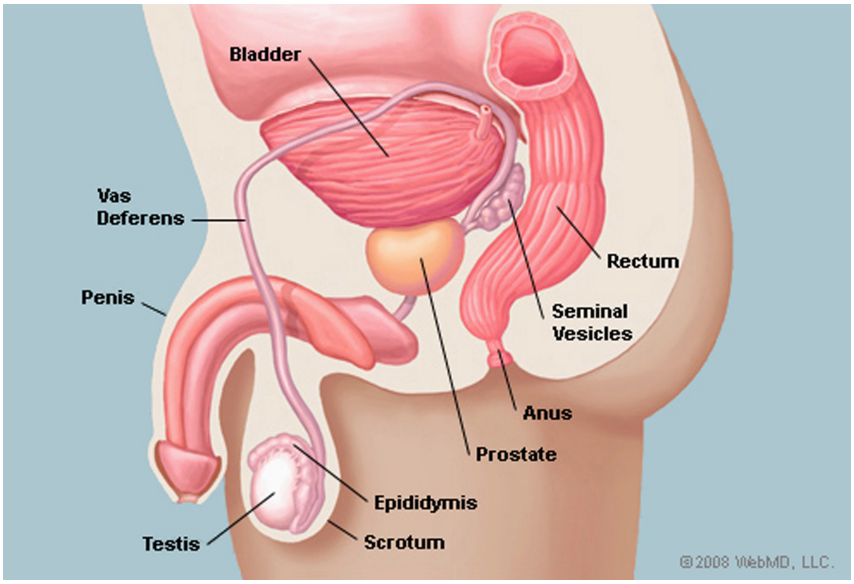

Figure 2.15: Prostate anatomy[1].

[1]Picture of the Prostate. Digital image. WebMD, 2009. Web. 7 July 2011.

95 % of all prostate carcinomas are adenocarcinomas. The degree of malignity of an adenocarcinoma is stated by use of different grading and staging schemes. The Gleason grading scheme provides information about the microscopic appearance of the tumor. The Gleason scale extends from 1 to 5, where a Gleason grade 1 tumor resembles normal prostate tissue and a Gleason grade 5 tumor shows undifferentiated cancer cells. The tumor's two most prominent structures are rated to account for different Gleason patterns within the carcinoma and summed up to the Gleason Score, which consequently ranges from 2 to 10. The higher the Gleason score the higher is the rate of growth and the probability for extra-capsular extension and metastasis of the tumor [7].

Another method for tumor staging is TNM staging, where the risk for lymph node metastasis and distant metastasis is also assessed. T describes the size and location of the primary tumor (see Fig. 2.16), N the involvement of regional lymph nodes and M distant metastasis [7, 24].

The treatment options for prostate cancer are watchful waiting, surgery, brachytherapy and external beam radiotherapy, depending on the staging of the tumor. Treating prostate cancer with IMRT offers the advantage of higher doses for improvement of cancer control rates beside a reduction of side effects induced through the treatment [25].

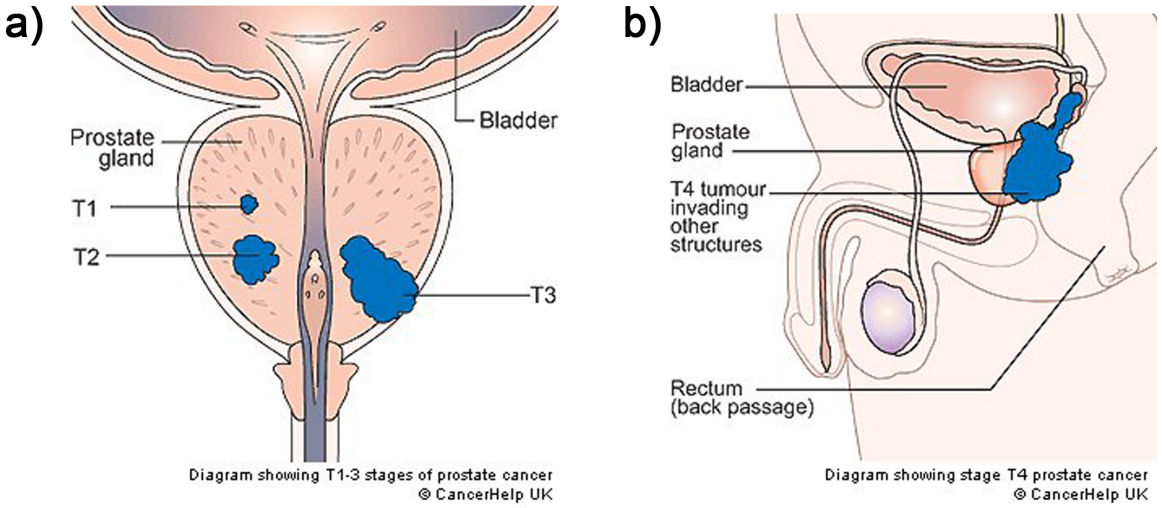

Figure 2.16: T(umor) staging of prostate cancer: a) T1-T3[1] and b) T4 [2].

[1]Diagram showing T1-3 stages of prostate cancer. Digital image. CancerHelp UK. Web. 7 July 2011.

[2]Diagram showing stage T4 prostate cancer. Digital image. CancerHelp UK. Web. 7 July 2011.

3 Material and Methods

3.1 Position Verification for Prostate Cancer Treatment

3.1.1 Gold Markers

Using bony landmarks for aligning the patient before an IGRT treatment fraction turned out to be not the optimum in case of prostate cancer irradiation. In other words, due to the varying position of the prostate gland with respect to bony anatomy caused by differing filling of the proximate organs rectum and bladder, a positioning based on bony landmarks introduces quite remarkable uncertainties limiting dose escalation [26]. Concerning the fact that the prostate gland cannot be represented on MV images and planar kV images because of the limited soft tissue contrast of the modalities, other techniques were established. The most promising ones in terms of workflow at the linear accelerator are the implantation of radio-opaque markers into the prostate in combination with kV-imaging [26–32], the implantation of electromagnetic transponders [33] and the use of CBCT scans [26, 32, 34].

Tracking the prostate's motion by utilization of electromagnetic transponders requires equipment, which is not available at the Medical University of Vienna/AKH. The daily use of CBCT scans causes a quite high extra dose burden [35] and is in comparison to kV-imaging using fiducial markers more time-consuming and needs more physician input [32]. Hence the intrafraction prostate motion was investigated by use of three implanted gold markers in combination with stereoscopic imaging (see section 3.1.2) in this study [36, 37]. Three fiducial gold markers with 1.2 mm diameter and 3 mm length (comparable to Fig. 3.1) distributed by CP Medical, Inc., were implanted transperineally into the prostate of each patient by use of mask narcosis and transrectal-ultrasound and C-arm-fluoroscopy guidance. One marker was placed in the apex of the prostate and the remaining two ones at the base of the prostate (close to the bladder). The procedure was performed 3 to 4 weeks in advance of planning CT and treatment start to account for possible induced oedema of the prostate right after insertion [26].

3.1.2 BrainLAB ExacTrac

ExacTrac is a system for stereoscopic radiographic imaging in the treatment room. It uses two kV X-ray tubes, mounted in the floor, that project on two opposite 20 x 20 cm^2 flat panel detectors, which are mounted on the ceiling (see Fig. 3.2). The setup geometry provides a distance from the X-ray tube to the detector on the opposite side of approximately 360 cm and

Figure 3.1: Fiducial gold markers used for target localization[1].

[1]IZI Gold Fiducial Markers. Digital image. IZI Releases New Product Lines! IZI Medical Products. Web. 22 July 2011.

a distance of 234 cm from the X-ray tube to the isocenter of the linear accelerator. Stereoscopic images acquired with ExacTrac allow patient positioning based on bony landmarks or implanted markers. The precision of a stereoscopic patient setup according to the prostate's position determined through fiducial markers in the target organ is equal to the precision of a setup based on 3D images as Logadóttir et al. reported [37].

For controlling the position of the treatment couch in real-time an infrared (IR) tracking system consisting of two IR cameras and one video camera is also included in the setup. With IR-reflecting markers on the skin of the patient or a reference star mounted on the couch, the couch movement for initial setup and position correction is steered [19].

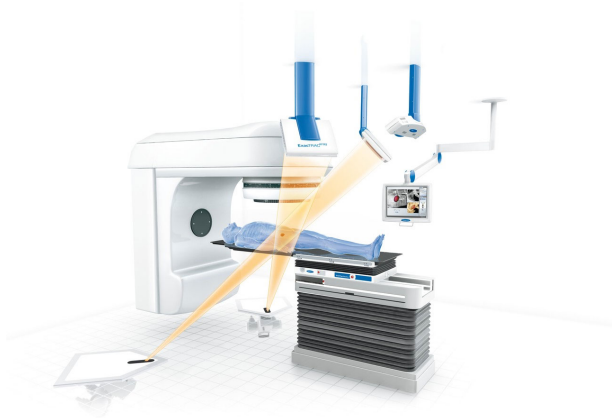

Figure 3.2: Setup of the ExacTrac system[1].

[1]ExacTrac® System. Digital image. ExacTrac® IGRT General Overview. Brainlab. Web. 14 May 2010.

Definition of Directions and Axes of Rotation

The coordinate system used for monitoring the patient has its origin in the isocenter of the linac. The **vertical** axis (z-axis in Fig. 3.3) states a displacement in anterior-posterior direction. Above the isocenter is the positive region, underneath the negative. The **lateral** axis (x-axis in Fig. 3.3) states sinister-dexter displacements with the positive range being sinister (towards tube 2) and the negative range being dexter (towards tube 1) from the isocenter. The **longitudinal** axis (y-axis in Fig. 3.3) goes alongside with the 0°-position of the treatment couch and states a displacement in cranial-caudal direction. The range from the isocenter towards the linac is defined as positive, the direction away from the linac as negative.

The **vertical** angle states a rotation around the vertical axis, which is strictly speaking a **table rotation** and defined as positive, when it is counterclockwise. A rotation around the longitudinal axis, also called a **roll** (defined as positive when right side up, left side down from the patient's point of view), is stated through a **longitudinal** angle. The **lateral** angle states a rotation around the lateral axis, which is also called **tilt** (defined as positive when head up, feet down from the patient's point of view) [31, 38]. At the Elekta Precise linac utilized for this study rotational errors can be measured through the ExacTrac system, but not corrected.

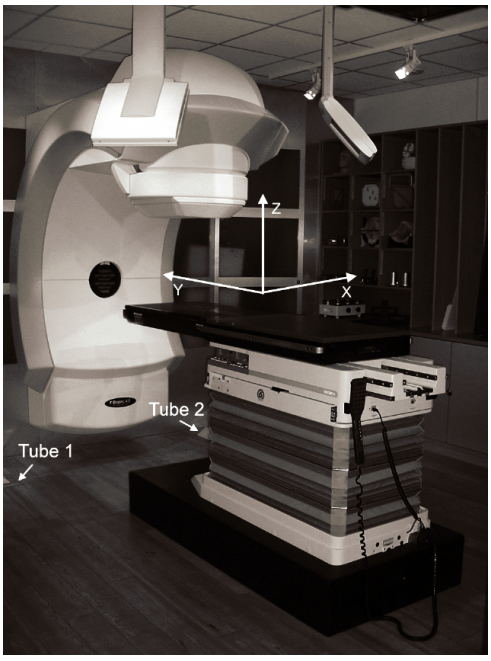

Figure 3.3: Definition of axes at the ExacTrac system (from [38]).

Table 3.1: Patient statistics.

	$P_{No.}$	Age [yrs]	BMI	T	$a/b/c$	N	M	GS	PSA [ng/ml]	$+LN$ [%]	D_{Pro} [Gy]	D_{Pel} [Gy]
IMRT	1	66	37.9	3		x	x	6	58.0	38.7	78	50.4
	2	68	32.7	3		x	x	6	27.0	18.0	78	50.4
	3	84	27.8	1	c	x	x	7	12.7	18.4	78	50.4
	4	74	26.1	2	c	x	x	9	32.3	51.5	76	50.4
	5	77	27.7	2	a	x	x	7	17.0	21.4	78	50.4
	6	60	25.5	2	c	x	x	6	34.0	22.7	78	50.4
	7	72	25.1	1	c	x	x	6	15.8	10.5	78	50.4
	8	77	31.5	1	c	x	x	7	11.1	17.4	74	45.0
	9	73	28.4	2	a	x	x	8	7.6	25.1	78	50.4
	10	73	30.1	1	c	x	x	9	20.7	43.8	78	50.4
	11	73	23.4	2	a	x	x	7	26.4	27.6	78	50.4
	12	75	24.8	3	b	x	x	8	12.6	28.4	78	50.4
4field box	13	83	33.9	2		x	x	7			78	
	14	58	45.0	1	c	x	x	7	5.4	13.6	78	
	15	76	22.1	1	c	x	x	6	5.8	3.9	78	
	16	72	31.2	1	c	x	x	7	5.8	13.9	78	
	17	60	19.8	1	c	x	x	6	5.7	3.8	78	

3.2 Treatment Planning

17 patients with localized prostate cancer treated with radiotherapy at the Medical University of Vienna/AKH from October 2010 to May 2011 were included in this study. Treatment technique, patient number ($P_{No.}$) and age, body mass index (BMI), TNM staging, Gleason score (GS), initial prostate-specific antigen level (PSA), risk for pelvic-lymph-node metastases ($+LN$) and dose prescription for PTV prostate (D_{Pro}) and PTV pelvis (D_{Pel}) for each patient are shown in table 3.1. Patients with an increased risk for pelvic-lymph-node metastases $+LN > 15$ % determined through Roach formula [39]

$$+LN = 2/3 \cdot PSA + (GS - 6) \cdot 10 \tag{3.1}$$

received an IMRT treatment where the pelvic lymph nodes were irradiated additionally. For patients with a risk for pelvic-lymph-node metastases below 15 % PTV prostate were treated with a four-field box technique.

Patients were scanned in supine position with a knee support in a Siemens Somatom Plus 4

Volume Zoom CT, Erlangen, one to two days before treatment start. Supine positioning is favorably in terms of patient comfort, prostate movement and dose levels for small bowel, rectal wall and bladder wall as Boehmer et al. reported. The additional use of a knee support reduces the dose to the rectum significantly compared to a setup without a knee support [26]. A slice thickness of 2 mm was chosen for a sufficient detection of the markers. Furthermore, the patients were told to have a comfortably filled bladder and an empty rectum.

Additionally, a 40 cc endorectal balloon (ERB) (Nordmann, Rüsch AG, Kernen, Germany) was used to spare the rectal wall and to immobilize the prostate (see Fig. 3.4). Smeenk et al. [40] reported reduced rectal and anal wall doses in planning studies when using an ERB, but results of comparative clinical studies are still required. An issue is a possible relaxation after the insertion of the ERB, which might occur when irradiation of the patient has already started. Therefore, the immobilizing properties of the ERB should be further investigated, as well as the interfraction reproducibility of its position and shape. According to Both et al. [41] an ERB reduced the prostate motion in all directions except for the lateral direction, where the prostate motion is the smallest anyway, in comparison with a non-ERB setup for a mean treatment time of 4 minutes.

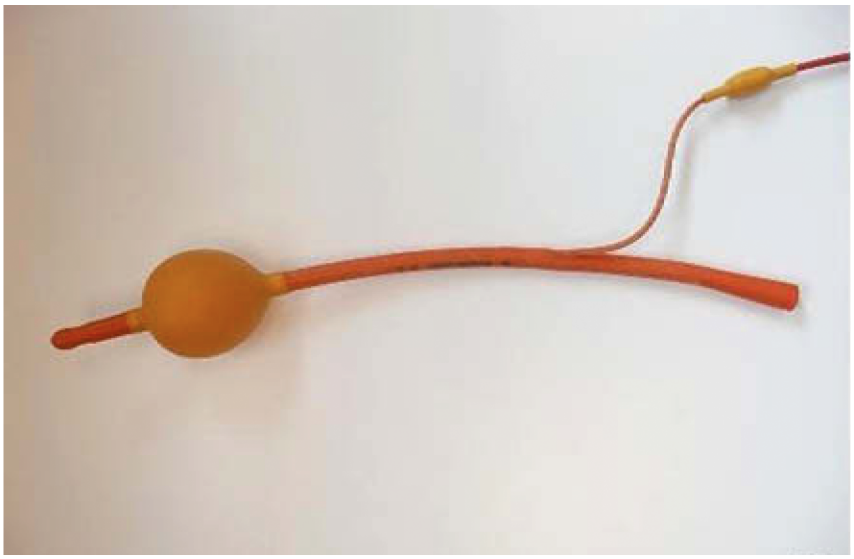

Figure 3.4: Endorectal balloon utilized for prostate immobilization and rectal wall sparing (from [40]).

All patients were treated with a prescribed dose of 78 Gy in 39 fractions, except for two IMRT patients receiving a dose of 76 Gy and 74 Gy, respectively.

Table 3.2: Dose-volume constraints for OARs for prostate IMRT up to 78 Gy.

	Rectum	Bladder	Femoral heads	Small intestine
V30Gy	-	< 80 %	-	-
V50Gy	< 50 %	< 50 %	< 5 %	< 15 %
V55Gy	-	< 45 %	-	-
V60Gy	< 45 %	-	-	-
V65Gy	< 40 %	-	-	-
V70Gy	< 20 %	< 20 %	-	-
D_{max}	< 85.8 Gy	< 85.8 Gy	< 60 Gy	< 56 Gy

For the IMRT patients a boost of 22 Gy was delivered to the PTV prostate in 11 fractions and for the remaining fractions the PTV consisted of prostate and pelvic lymph nodes.

The 4-field box treatment included a 10 Gy boost in 5 fractions. All fractions were delivered to the PTV prostate.

Isotropic margins of 10 mm were applied, except for the boost where the margin in posterior direction was 5 mm to spare the rectal wall, for both, IMRT and four-field box treatment.

For IMRT planning the Monaco V 2.0.4 planning system was utilized. For the beam energy 10 MV were chosen, the MLC width was 1 cm, the grid spacing 4 mm and the beams were arranged equidistantly. A plan was accepted when the criteria were met that 95 % of the PTV received at least 95 % of the prescribed dose, the dose maximum was below 110 % and the medium dose below or equal 103 % of the prescribed dose and the dose constraints for OARs (see Tab. 3.2) were fulfilled.

The boost for the PTV prostate was performed as a 9-field IMRT for 3 patients and then changed to the new clinical standard, a 5-field IMRT, for the last 9 patients. The irradiation of the PTV including the prostate and the pelvic lymph nodes was delivered through a 9-field IMRT, where the prostate (with a CTV to PTV margin of 10 mm) received a simultaneous integrated boost of 56 Gy and the pelvic PTV a dose of 50.4 Gy in 28 fractions. Sample dose distributions for 5-field boost IMRT, 9-field pelvic IMRT and 4-field box treatment are shown in Fig. 3.5.

3.3 Treatment Fractions

All treatments were performed with an Elekta Precise linac (see Fig. 3.6). For every fraction the patients were immobilized in supine position utilizing a knee support on the treatment couch

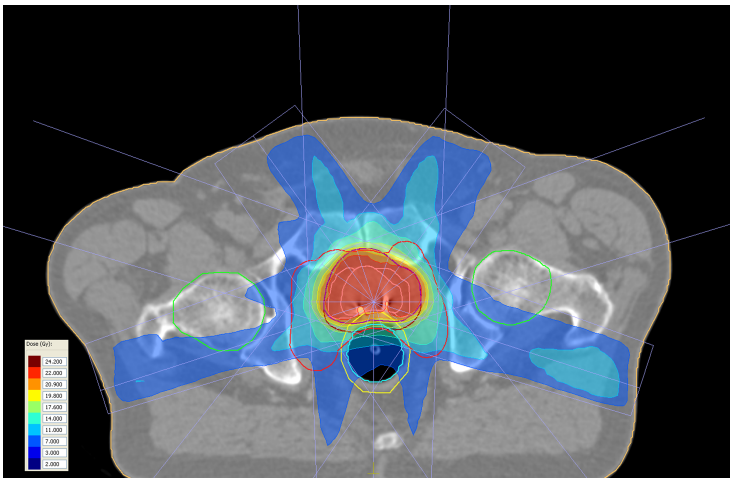

(a) 5-field boost IMRT

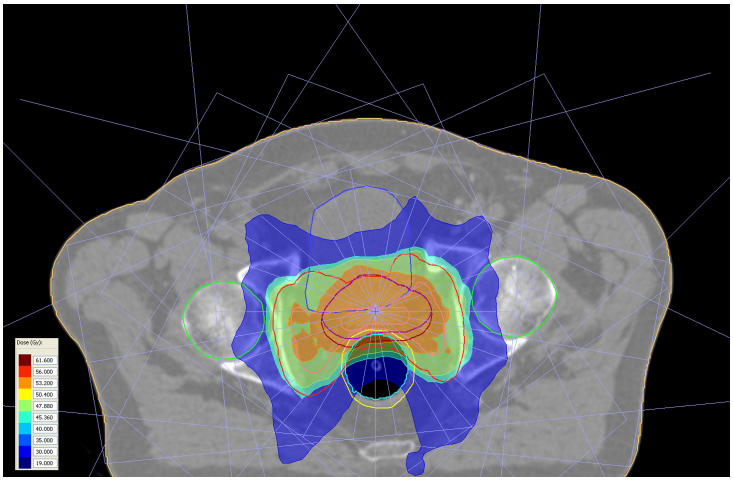

(b) 9-field pelvic IMRT

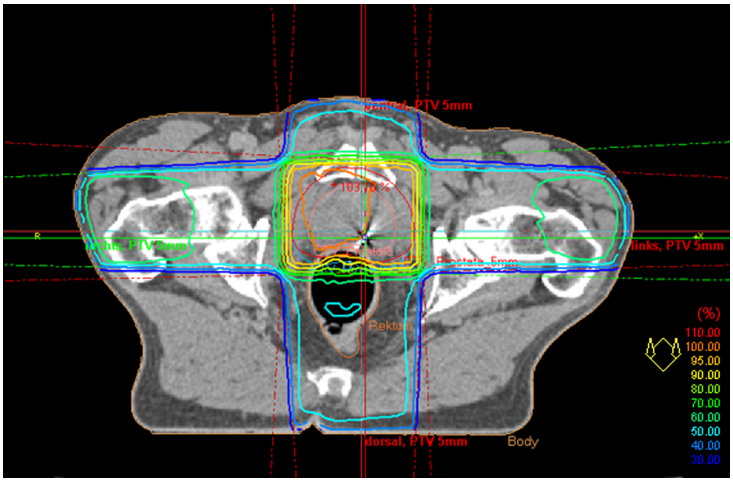

(c) 4-field box

Figure 3.5: Sample treatment plans.

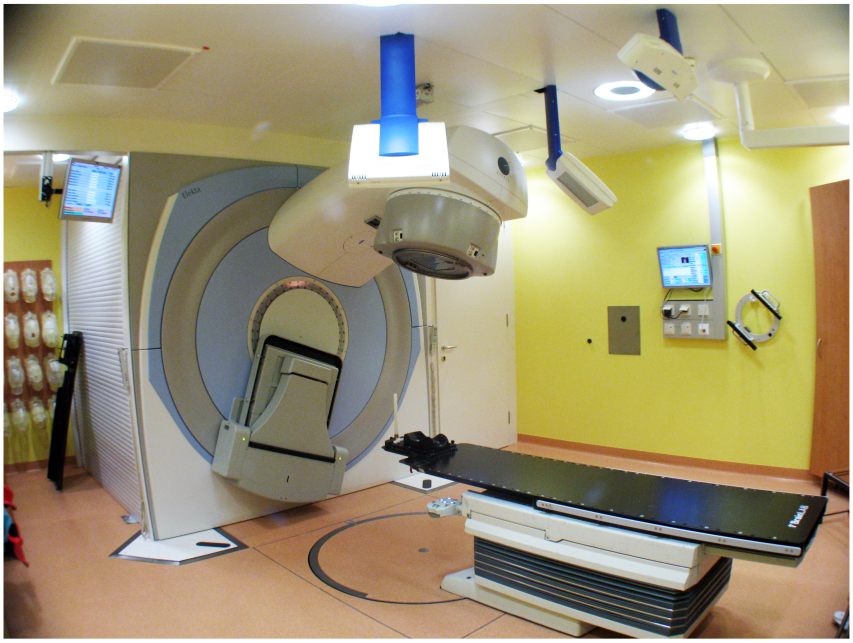

Figure 3.6: Linac and ExacTrac system at the Medical University of Vienna/AKH.

according to the clinical protocol. As for planning they were told to have a comfortably filled bladder and an empty rectum. The 40 cc endorectal balloon was daily inserted into the rectum.

The boost fractions, where the PTV and the margin in posterior direction were smaller and therefore the immobilization of the prostate was crucial, were scheduled as the first 11 fractions within the treatment series to tackle the issue that particular patients could not bear the balloon after some fractions.

Imaging and Setup Protocol

After the first setup based on skin marks utilizing the in-room lasers, the patients were imaged using the ExacTrac (BrainLAB AG, Feldkirchen, Germany) stereoscopic imaging system (see Fig. 3.7). Depending on the figure of the patient the protocol "Abdomen Standard" (120 kV, 160 mA, 130 ms) or the protocol "Abdomen Heavy" (145 kV, 160 mA, 160 ms) was chosen.

The couch movement for initial setup and position correction was controlled through an infrared tracking system using a reference star mounted on the couch.

For position verification the ExacTrac images were fused with reconstructions of the planning CT and, based on this information, the correction for the couch position was calculated automatically. For the prostate cancer patients evaluated in this work the fusion was carried out according to the position of the three gold markers within the prostate. Generally, the markers,

(a) right posterior oblique (b) left posterior oblique

Figure 3.7: Images acquired with the ExacTrac system showing fiducial markers and the endorectal balloon.

which have to be defined once in the planning CT data, are detected through the system and the corresponding values of displacement, which are the basis for couch movement, are stated. A problem occurred when the markers were placed inappropriately (too close to each other) or migrated. Then the automatic detection did not work. The fusion had to be carried out manually and the RTTs had to compromise about the best match for all 3 markers. In this case positioning was not that accurate, because an optimal match was not possible. Also, the system did not deliver any values for rotation.

The imaging data of each fraction was stored and provided the possibility of a retrospective adjustment based on other quantities, like bony landmarks or the endorectal balloon.

The treatment couch was shifted manually, when the translational error in one or more directions exceeded a tolerance limit, which was 3 mm for this study as this is the standard for clinical practice. If the patient had to be shifted, verification images were acquired and if the displacement for all directions was within the tolerance limit, the irradiation was started. Using the ExacTrac system, images can be taken also during the treatment, but one has to consider that at gantry angles different from 0° the gantry may interfere with the image-taking process.

To evaluate intrafraction motion the patients were imaged during (approximately at halftime) and after the treatment for IMRT fractions in order to obtain a time trend of the current position of the prostate and the bony anatomy. For the 4-field box fractions imaging was performed just after the treatment. 3-4 image pairs were acquired in every IMRT fraction and 2-3 ones in every

4-field box fraction, respectively. The average time requirement for imaging was approximately 5 min.

In exceptional cases, where the displacement of the patient after the first setup correction utilizing the ExacTrac system still exceeded the 3 mm tolerance, another correction was performed and a verification image pair taken. Owing to these circumstances the overall number of image pairs per fraction increased to more than 4 for IMRT and more than 3 for 4-field box. Marker/prostate and bone drifts were evaluated as a function of treatment time for 587 treatment fractions, where the prostate motion was obtained from the gross marker motion through subtracting the bone motion.

As the reproducibility of the endorectal balloon's position is an issue, the position of the balloon in relation to its position in the planning CT was investigated as well. The balloon is perfectly represented on the images acquired with the ExacTrac system (see Fig. 3.7), but unfortunately not visible at all on the reconstructed images from the planning CT used for fusion. As a retrospective delineation of the balloon was impossible, the balloon was delineated in the planning CT data for 4 additional patients. The fusion of the images was carried out manually based on the position of the balloon to gain values for the displacement of the balloon with respect to bony anatomy.

3.4 Margin Calculation

Margins accounting for the remaining positioning errors after setup correction and intrafractional prostate and whole-patient motion were calculated based on the values for displacement after treatment delivery according to the van Herk formula (see equation 2.17) [20] for IMRT boost, IMRT pelvic and 4-field box fractions, respectively.

4 Results

More than 2100 image pairs for 587 treatment fractions acquired with the ExacTrac system were evaluated as a function of treatment time. 413 IMRT fractions and 174 4-field box fractions were investigated.

4.1 IMRT Treatment

Mean treatment delivery time, number of fields, number of segments and monitor units (MUs) for the boost and pelvic IMRT of each patient can be seen in Tab. 4.1. In Fig. 4.1 the intrafraction whole-patient displacement for 5-field and 9-field IMRT fractions is shown as a function of treatment time. Each type of colored symbol represents the data concerning one patient. The initial bony anatomy position was assumend to be zero in lateral, longitudinal and vertical direction, respectively. Images were acquired before, during and after a treatment fraction. Hence one has to keep in mind that it is impossible to track each single movement of bones or prostate with this method. The positions of bones and markers in the images represent just snapshot, but taking many snapshots at random positions gives an estimation of the real long-term intrafraction motion. However, short-term variations in the order of seconds cannot be traced [28, 42].

Having a closer look at Fig. 4.1 it is apparent that whole-patient motion is strongly patient dependent (e.g. the patient represented through red triangular symbols was moving quite extensively compared to other patients). In lateral direction (see Fig. 4.1(a)), meaning that the patient is moving to the right (-) or to the left (+), the largest displacement was 11 mm. The patients depicted by the smoky blue diamond and the red triangle moved more than the others. In longitudinal direction (see Fig. 4.1(b)), where (+) states a motion in cranio-caudal direction towards the linac and (-) from the linac away, bone movement was the smallest, but again for the patient symbolized through the red triangular symbol in the majority of cases the largest. The largest value measured in longitudinal direction was 4 mm. In vertical direction (see Fig. 4.1(c)), meaning a motion in anterior-posterior direction where the patient is moving his hips up (+) or down (-), the largest displacement of 12 mm for the whole series was measured. For motion in vertical direction the patient represented by red triangles was remarkably outstanding because of consistently much larger bone drifts as for all other patients, who seemed to move slightly down during a fraction.

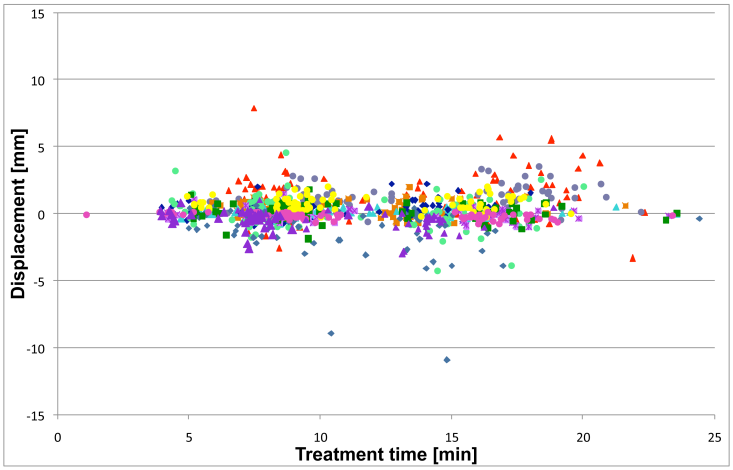

(a) lateral direction

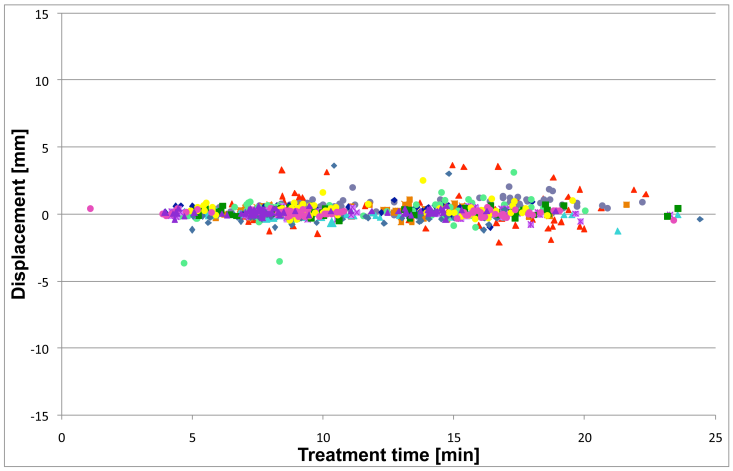

(b) longitudinal direction

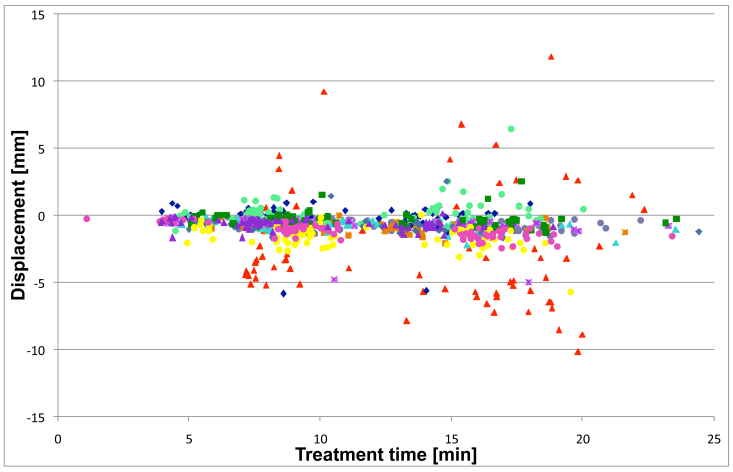

(c) vertical direction

Figure 4.1: Net bone drifts for IMRT treatments: images were taken at half-time and at the end of a fraction and corrected for the position of bony anatomy at the begin of the fraction right before irradiation start.

Table 4.1: Number of fields, number of segments, MUs and mean treatment delivery time t for boost and pelvic IMRT treatment of each patient.

$P_{No.}$	Boost IMRT				Pelvic IMRT			
	Fields	Segments	MUs	$t[min]$	Fields	Segments	MUs	$t[min]$
1	9	74	557	16.9	9	96	602	18.0
2	9	50	472	15.2	9	100	716	18.0
3	9	46	441	13.0	9	72	477	14.3
4	5	42	391	12.2	9	87	533	17.5
5	5	29	354	9.2	9	70	515	14.6
6	5	34	373	9.8	9	74	602	15.9
7	5	29	332	7.6	9	89	691	17.1
8	5	50	395	10.6	9	64	530	14.7
9	5	42	344	11.4	9	87	754	17.2
10	5	42	375	10.2	9	87	594	16.3
11	5	33	316	7.8	9	93	656	17.0
12	5	30	308	8.1	9	74	474	14.3

Net marker drifts were obtained through correction of the marker positions during and after the treatment for setup tolerance and whole-patient motion. In contrast to bone drifts, marker (i.e. prostate) drifts were less dependent on patients and showed a significant increase with treatment time in longitudinal and vertical direction (see Fig. 4.2). In lateral direction the prostate stayed rather stable for all patients in almost all fractions (see Fig. 4.2(a)). The largest motion in lateral direction occurred in a particular case and was of a magnitude of 7 mm. In comparison to the movement in lateral direction the motion in longitudinal direction (see Fig. 4.2(b)) generally was much larger, however, the peak value was also 7 mm. For the whole patient population it seemed that for longer treatment fractions the prostate moved slightly caudal during the treatment. The largest prostate motion was in general measured in vertical direction, with a maximum value of 8 mm (see Fig. 4.2(c)). Also, the prostate seemed to move slightly posterior for longer treatment fractions.

3D bone and marker drifts were calculated from the values for the single directions lateral, longitudinal and vertical (see Fig. 4.3). In general, the bone displacement increased as a function of treatment time and was strongly patient dependent (see Fig. 4.3(a)). The patient depicted by the red triangular symbols was again outstanding because of the largest deviations from his initial position with a peak value of 13 mm. On average the bony anatomy was shifted about

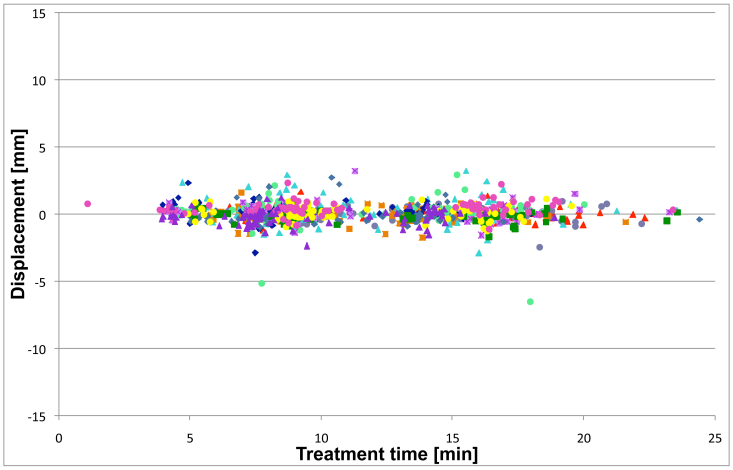

(a) lateral direction

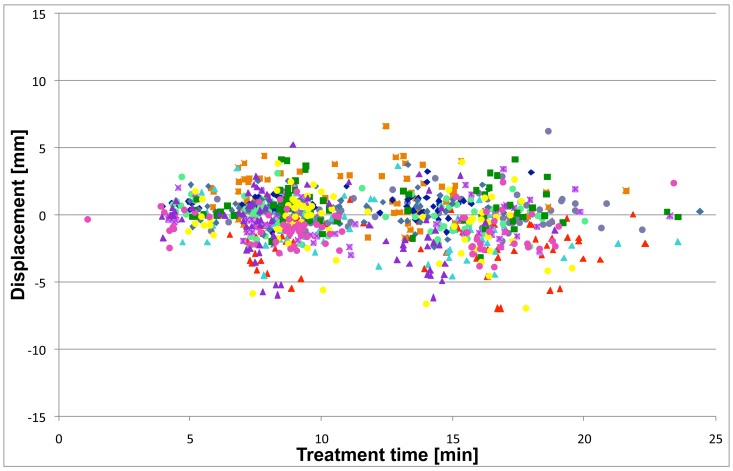

(b) longitudinal direction

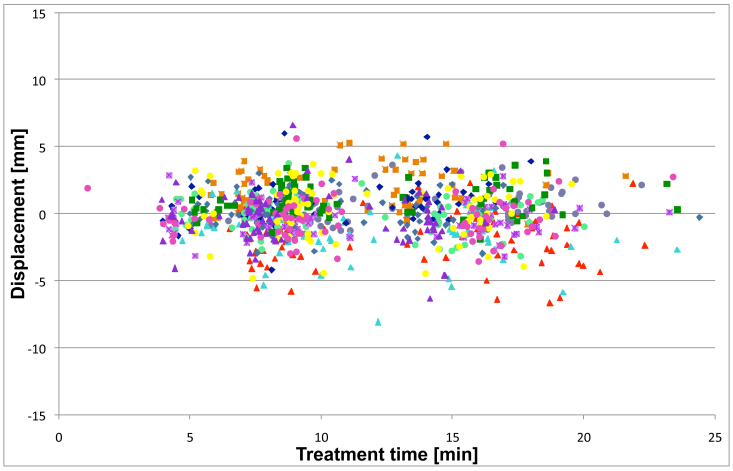

(c) vertical direction

Figure 4.2: Net marker drifts for IMRT treatments: images were taken at half-time and at the end of a fraction and corrected for whole-patient motion and setup tolerance.

2.5 mm in 20 min. In contrast to 3D bone drifts, 3D marker drifts were less patient dependent and showed a much uniformer distribution with respect to the values for single patients (see Fig. 4.3(b)). The maximum value of 9 mm achieved for marker drifts was remarkably smaller than the peak value for the whole-patient motion, although the average 3D marker drift was about 3 mm after 20 min treatment time.

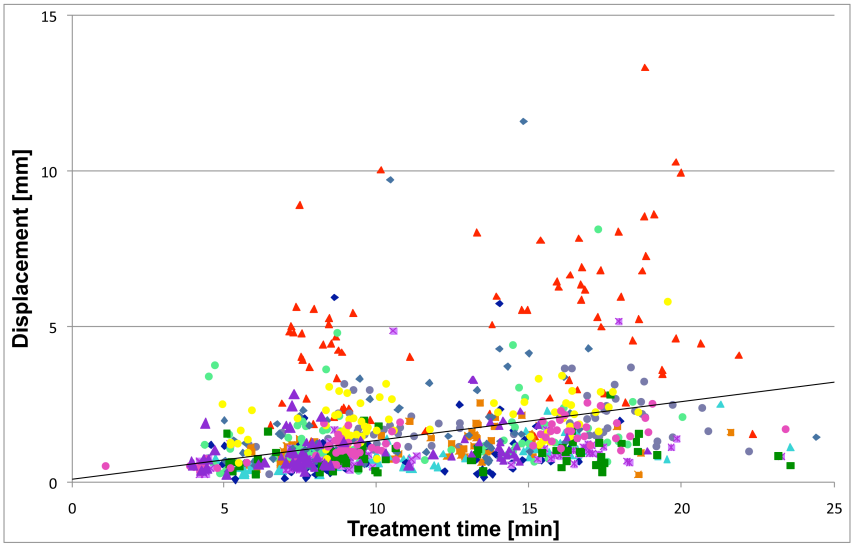

(a) 3D bone drifts

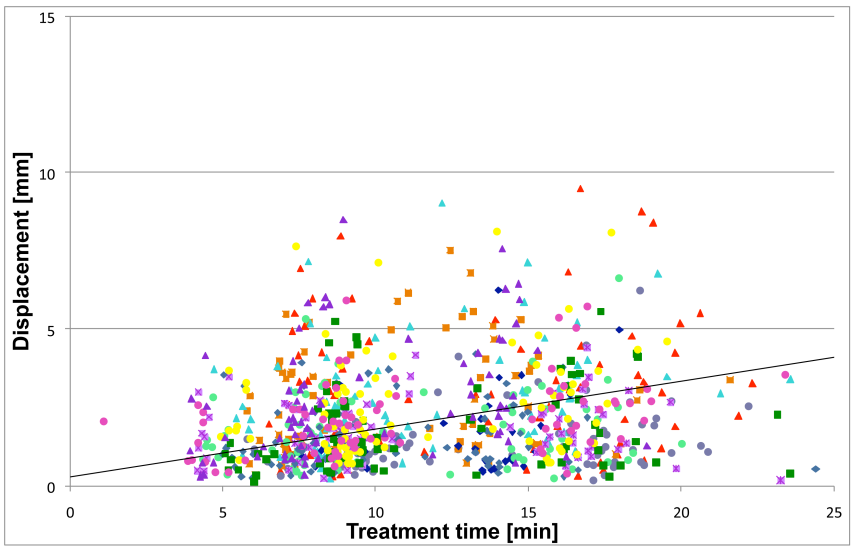

(b) 3D marker drifts

Figure 4.3: Comparison of 3D bone and marker drifts for IMRT treatments.

Trends for standard deviations of prostate and patient motion are shown in Fig. 4.4 and Fig. 4.5. Every point in the figures represents the standard deviation before, during or after

a treatment fraction for a single patient and all treatment fractions of one type. The light green dots represent the 5-field boost IMRT fractions characterized through shorter treatment times (the maximum average treatment time was 12 min) compared to the 9-field pelvic IMRT fractions, symbolized through blue squares, with a maximum average treatment delivery of about 18 min.

The SD for the bone drifts was following the trend line about 1.2 mm after a treatment time of 18 min in lateral direction (see Fig. 4.4(a)). On average the largest bone movement occurred in lateral direction. A value of 3.1 mm was obtained as the largest SD after treatment for a patient receiving a 5-field boost treatment series. The smallest bone motion occurred in longitudinal direction (see Fig. 4.4(b)), where the maximum value of about 1.2 mm for the SD of the bone shift after treatment delivery was again obtained for a 5-field boost treatment series. Following the trend line for longitudinal direction the SD resulted in a value, slightly larger than 0.5 mm after a treatment time of 18 min. The largest SDs of the bone drift during and after treatment delivery were measured in vertical direction with values of about 2.9 mm and 3.6 mm, respectively, for a patient receiving a 9-field pelvic IMRT (see Fig. 4.4(c)). According to the trend line the average SD after a treatment time of 18 min is about 1 mm.

As the tolerance for patient positioning was 3 mm in every direction an initial SD occured for the prostate's position in every direction (see Fig. 4.5). In lateral direction the average initial SD of the prostate's position was lowest and about 0.8 mm (see Fig. 4.5(a)). For longer treatment times up to 18 min there was only a slight increase to about 1 mm. The peak value for the SD of the marker positions in lateral direction was 1.5 mm. In longitudinal direction the initial average SD of the markers' position resulted in about 0.9 mm (see Fig. 4.5(b)). Over the treatment time it showed a much steeper increase than for lateral direction to about 1.8 mm at a time of 18 min. The maximum value for the SD of the prostate's position resulted in approximately 2.6 mm. The average SD for the prostate's position before irradiation start was the largest in vertical direction, reaching a value of about 1.2 mm (see Fig. 4.5(c)). For longer treatment times it increased steepest to about 2.2 mm at a time of 18 min. Also, the peak value of the SD of the markers' position for a patient after 9-field pelvic IMRT delivery was the largest of the series, with a value of about 3.4 mm.

A comparison of the trend lines of the SDs of marker and bone drifts is shown in Fig. 4.6. Apparently the SDs for particular directions show different behaviour for prostate and bone motion, respectively. The SDs of the prostate's position started at larger values because of the

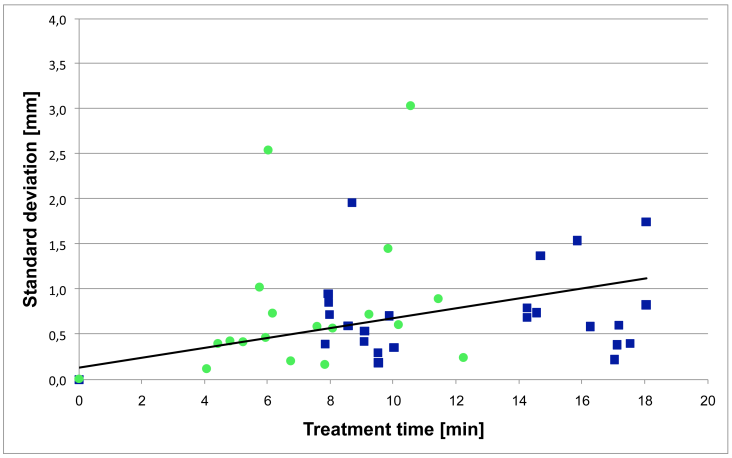

(a) lateral direction

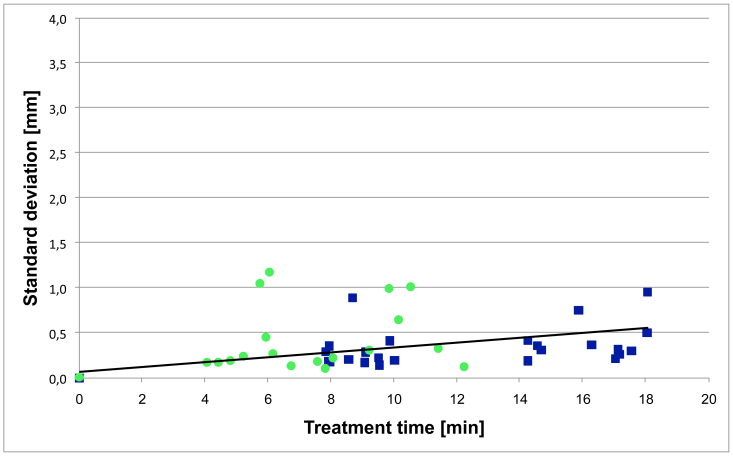

(b) longitudinal direction

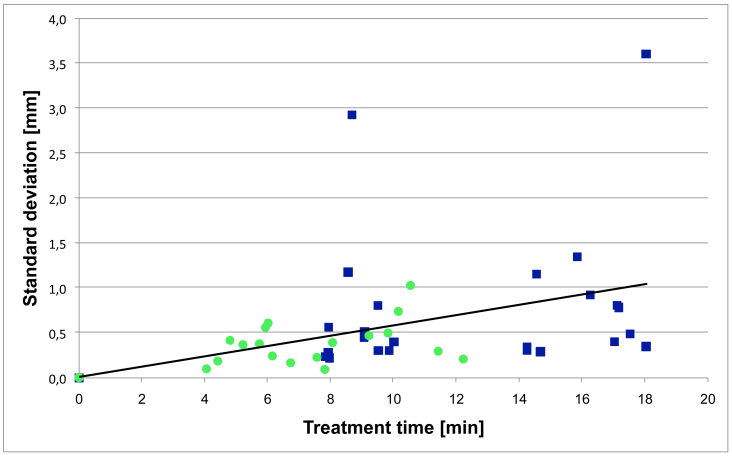

(c) vertical direction

Figure 4.4: Standard deviations of bone drifts for each IMRT patient before, during and after IMRT fraction with interpolated trend line. Green dots represent 5-field boost IMRT fractions and blue squares 9-field pelvic IMRT fractions.

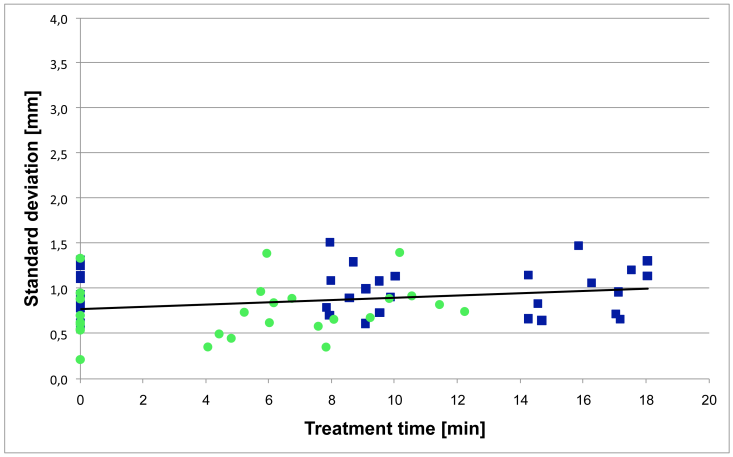

(a) lateral direction

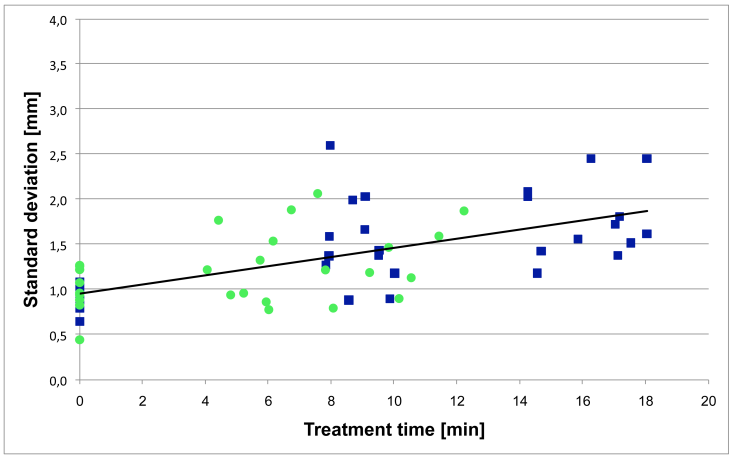

(b) longitudinal direction

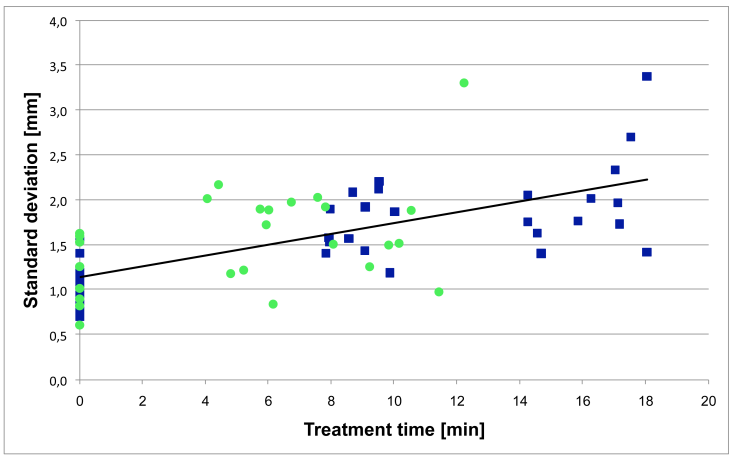

(c) vertical direction

Figure 4.5: Standard deviations of marker positions for each IMRT patient before, during and after IMRT fraction with interpolated trend line. Green dots represent 5-field boost IMRT fractions and blue squares 9-field pelvic IMRT fractions.

setup tolerance. For lateral direction the SD of the markers' position was lowest and was on average already exceeded by the SDs of the bone drifts in lateral and vertical direction at a treatment time of 18 min. Having a look at the SDs of the bone drifts, the lowest values were obtained in longitudinal direction.

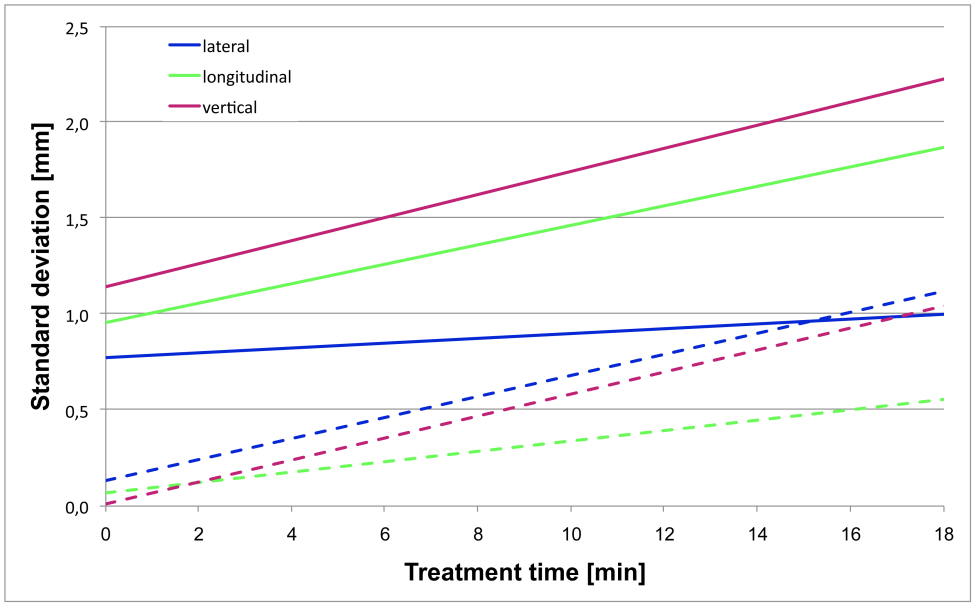

Figure 4.6: Standard deviations of marker drifts (solid lines) and bone drifts (dashed lines) as a function of treatment time for IMRT fractions in comparison. Initial standard deviations for marker drifts due to 3 mm setup tolerance.

The median, minimum, maximum and lower- and upper quartile values of the bone drifts after treatment delivery for all patients are shown in Fig. 4.7 and Fig. 4.8 for the boost IMRT fractions and the 9-field pelvic IMRT fractions, respectively. The values for the marker drifts after treatment delivery can be seen in Fig. 4.9 and Fig. 4.10 for the boost IMRT fractions and the 9-field pelvic IMRT fractions, respectively.

4.2 Four-Field Box Treatment

For four-field box treatments images were only taken in advance of irradiation start and after treatment delivery due to generally short treatment times (on average 5.4 min). In Fig. 4.11 the intrafraction whole-patient displacement for 4-field box fractions is shown as a function of treatment time. Net marker drifts for 4-field box treatments are displayed in Fig. 4.12, while Fig. 4.13 gives an overview of 3D bone and marker drifts.

In Fig. 4.14 the SDs of the bone drifts are shown for lateral, longitudinal and vertical direction, respectively. In lateral direction the SD for bone motion was the largest with a peak

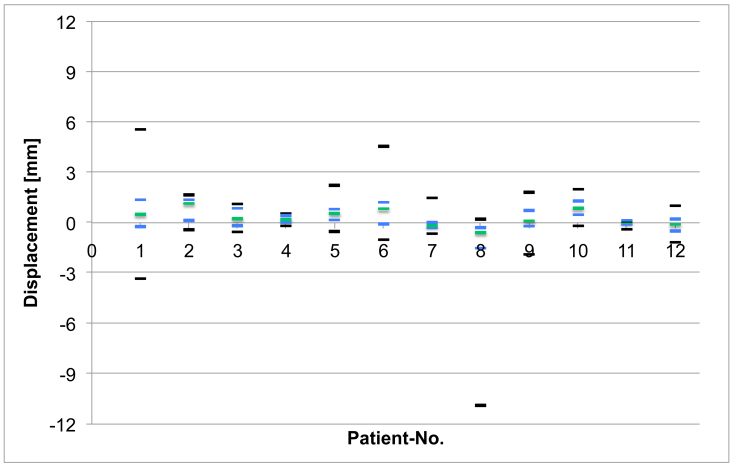

(a) lateral direction

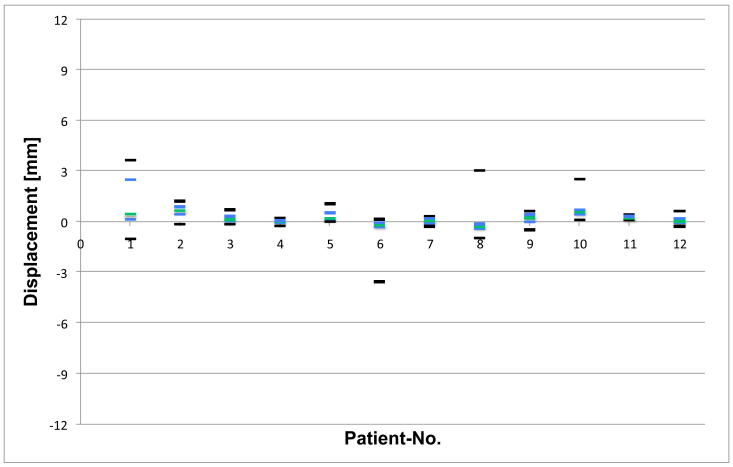

(b) longitudinal direction

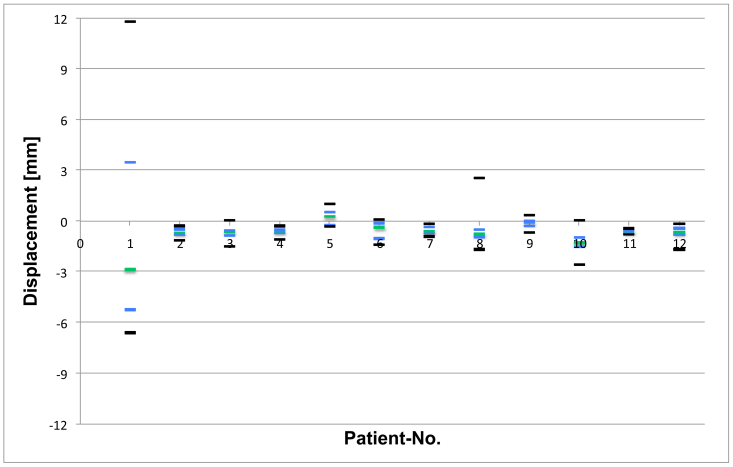

(c) vertical direction

Figure 4.7: Median, minimum, maximum and lower- and upper quartile values of the bone drifts after treatment delivery for all patients for boost IMRT fractions.

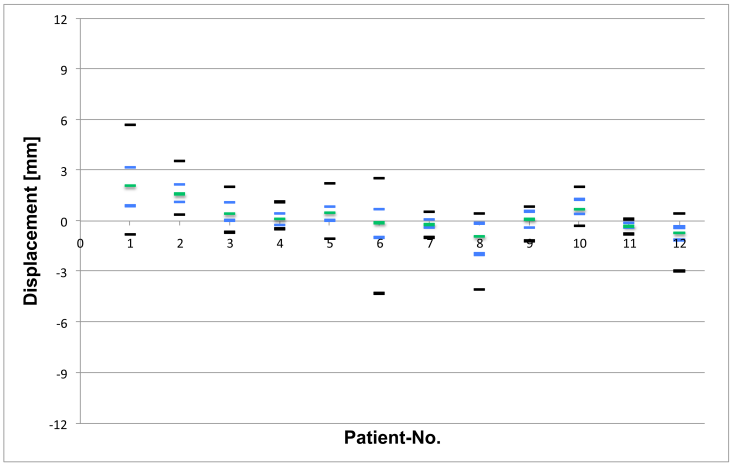

(a) lateral direction

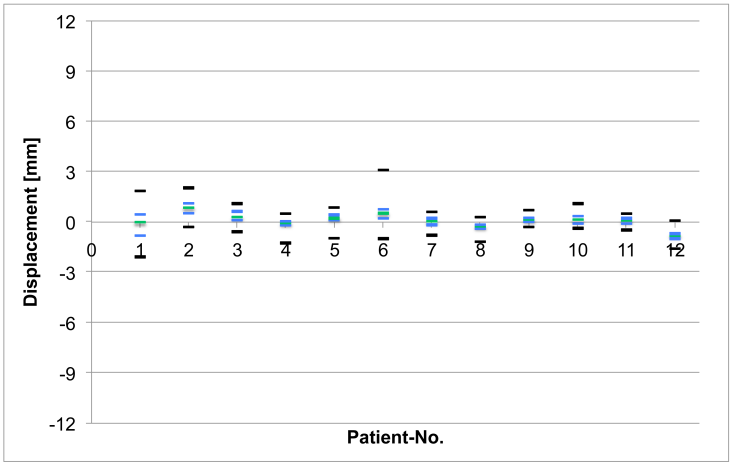

(b) longitudinal direction

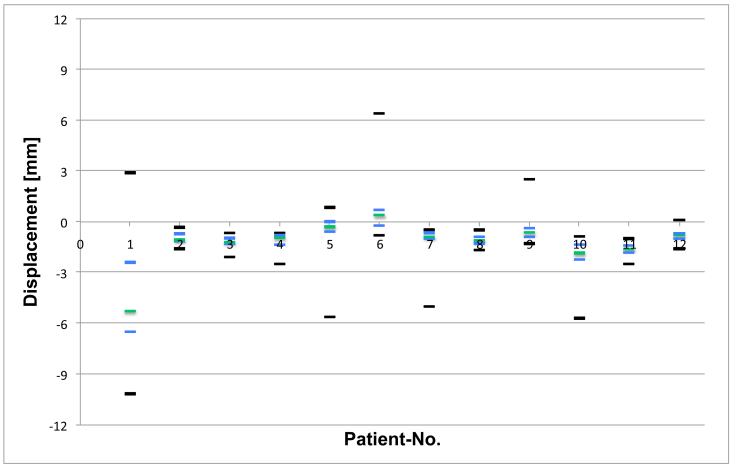

(c) vertical direction

Figure 4.8: Median, minimum, maximum and lower- and upper quartile values of the bone drifts after treatment delivery for all patients for 9-field pelvic IMRT fractions.

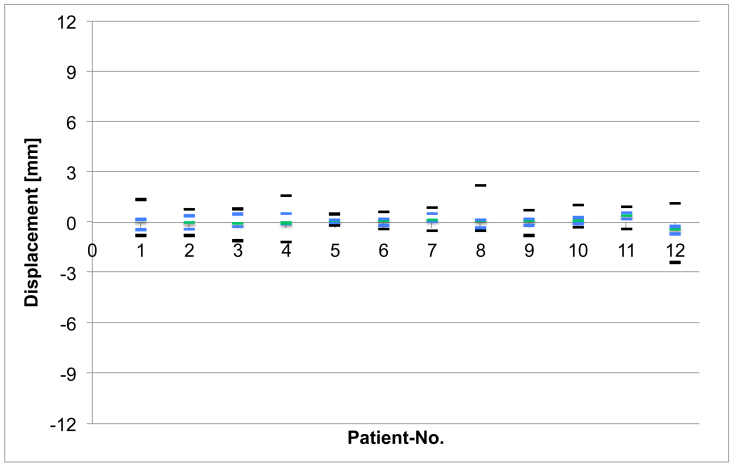

(a) lateral direction

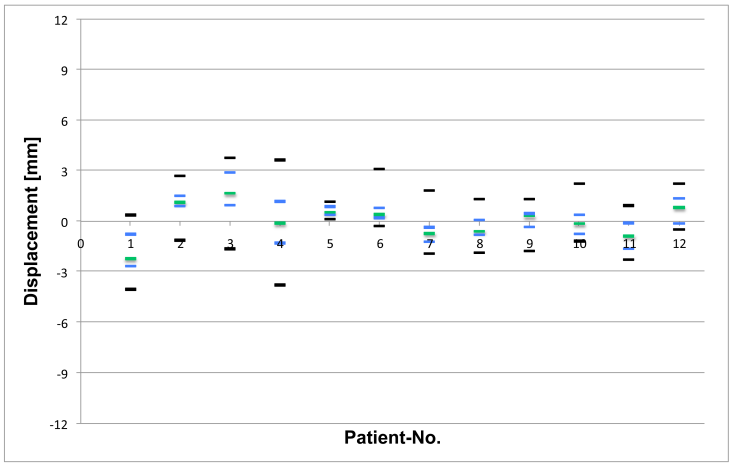

(b) longitudinal direction

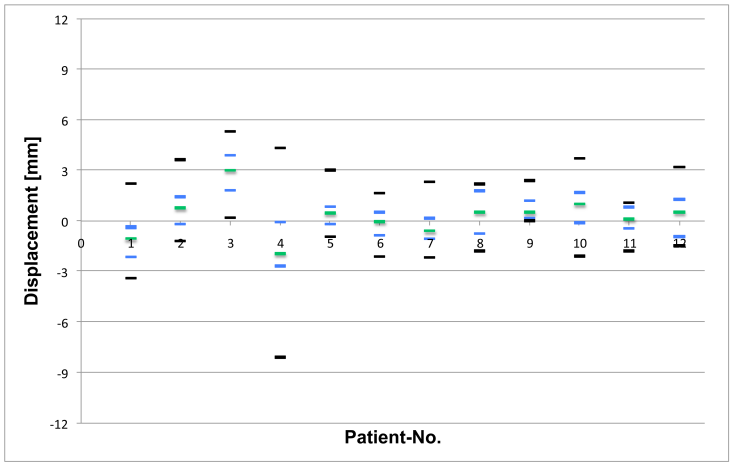

(c) vertical direction

Figure 4.9: Median, minimum, maximum and lower- and upper quartile values of the marker drifts after treatment delivery for all patients for boost IMRT fractions.

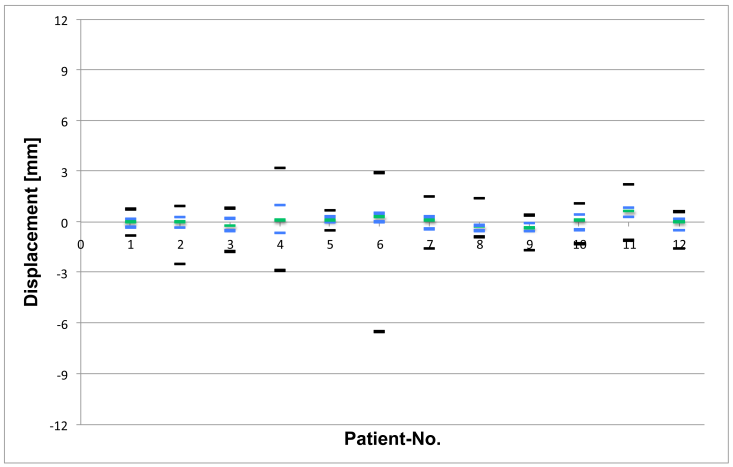

(a) lateral direction

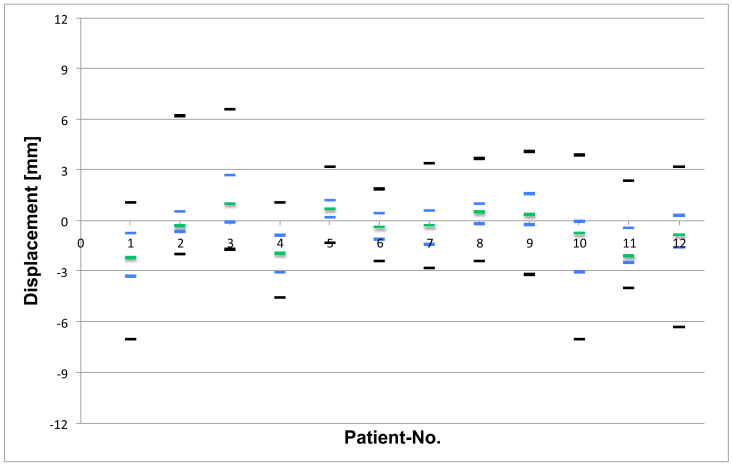

(b) longitudinal direction

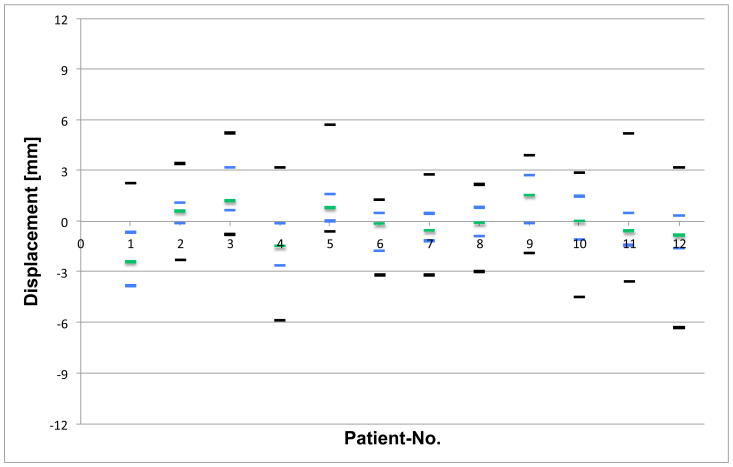

(c) vertical direction

Figure 4.10: Median, minimum, maximum and lower- and upper quartile values of the marker drifts after treatment delivery for all patients for 9-field pelvic IMRT fractions.

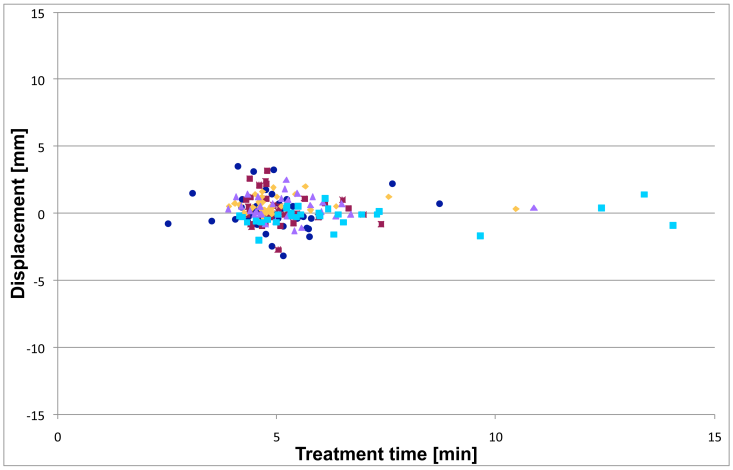

(a) lateral direction

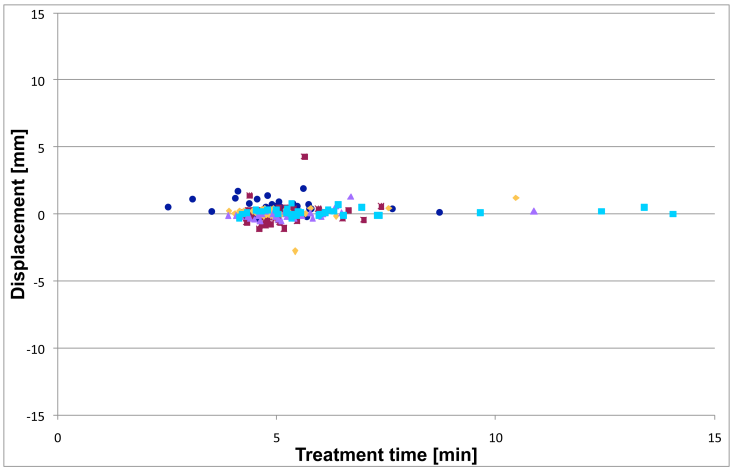

(b) longitudinal direction

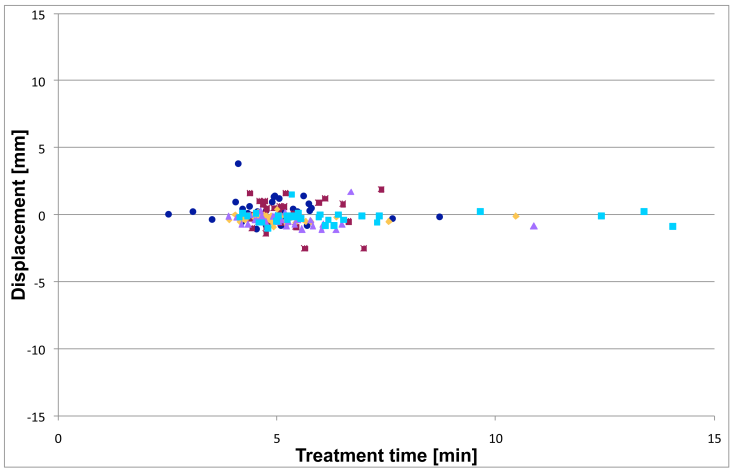

(c) vertical direction

Figure 4.11: Net bone drifts for 4-field box treatments: images were taken at the end of a fraction and corrected for the position of bony anatomy at the begin of the fraction right before irradiation start.

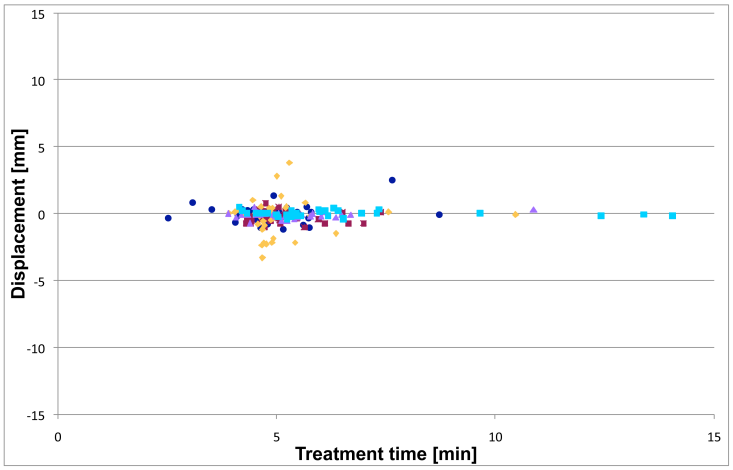

(a) lateral direction

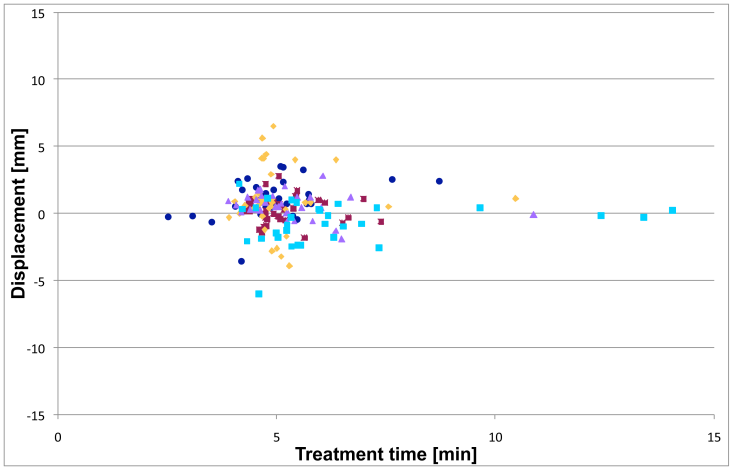

(b) longitudinal direction

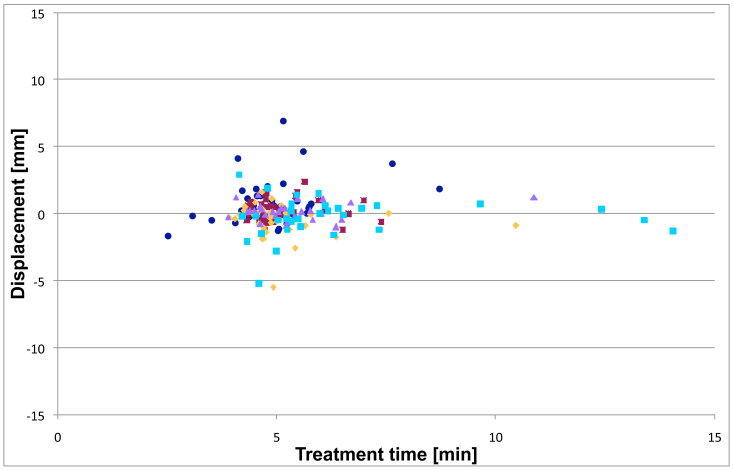

(c) vertical direction

Figure 4.12: Net marker drifts for 4-field box treatments: images were taken at the end of a fraction and corrected for whole-patient motion and setup tolerance.

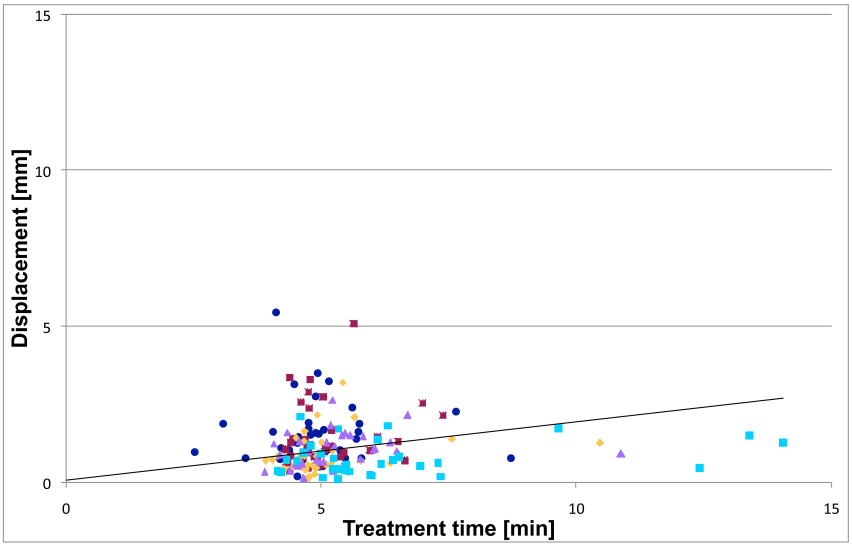

(a) 3D bone drifts

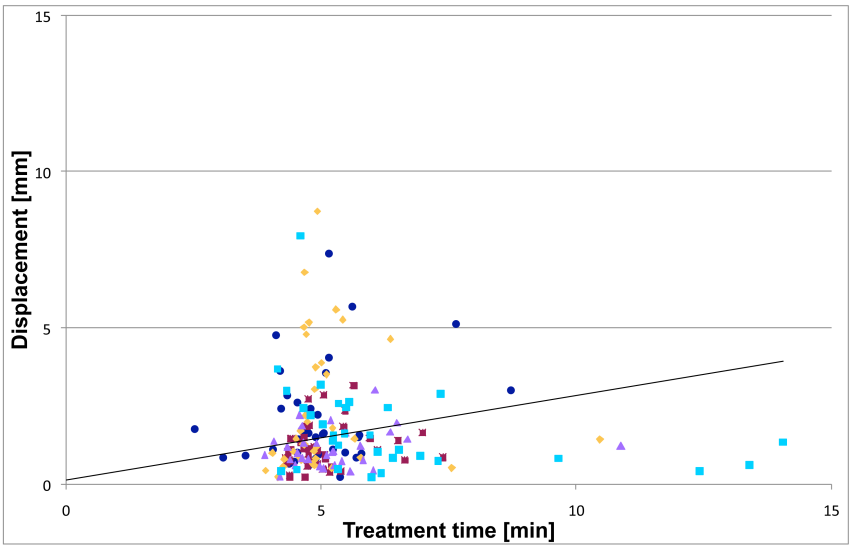

(b) 3D marker drifts

Figure 4.13: Comparison of 3D bone and marker drifts for 4-field box treatments.

value of about 1.4 mm. Following the trend line an average value of 1 mm was obtained at a treatment time of about 6 min (see 4.14(a)). In longitudinal direction the movement of bony anatomy was smallest with a maximum value of approximately 0.8 mm and an average value of about 0.5 mm at a treatment time of 6 min, gained through the trend line (see Fig. 4.14(b)). The peak value for the SD of bone motion in vertical direction resulted in about 0.9 mm (see Fig. 4.14(c)). Following the trend line for vertical direction an average SD of about 0.7 mm occured at a treatment time of about 6 min.

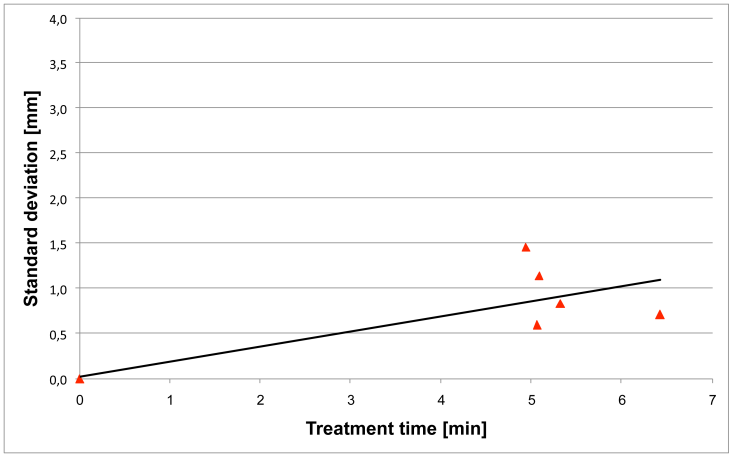

(a) lateral direction

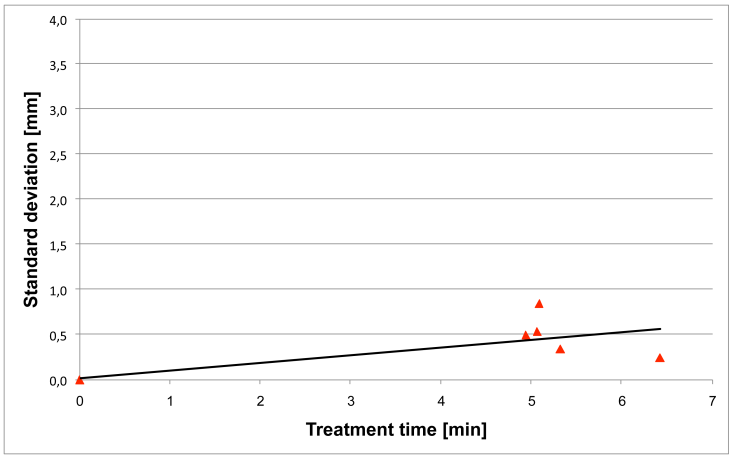

(b) longitudinal direction

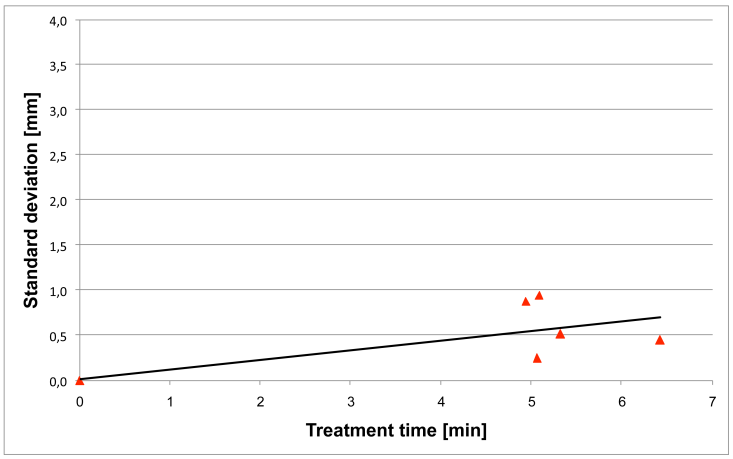

(c) vertical direction

Figure 4.14: Standard deviations of bone drifts for each 4-field box patient before and after treatment delivery.

Table 4.2: Bone intrafraction motion: group systematic error, M, standard deviation of the systematic error, Σ, and standard deviation of the random error, σ, for 5-field boost IMRT, 9-field pelvic IMRT and 4-field box treatments in lateral, longitudinal and vertical direction, respectively.

	5-field IMRT			9-field IMRT			4-field box		
[mm]	lat	long	vert	lat	long	vert	lat	long	vert
M	0.1	0.1	-0.5	0.2	0.2	-1.2	0.2	0.1	-0.1
Σ	0.7	0.3	0.4	0.9	0.3	1.1	0.3	0.2	0.2
σ	1.2	0.6	0.5	0.9	0.5	1.3	1.0	0.5	0.7

The initial SD of the prostate's position for four-field box treatments in Fig. 4.15 is due to the setup tolerance of 3 mm in every direction. The average initial SD of the prostate's position was about 1 mm in lateral direction (see Fig. 4.15(a)). Following the trend line an average value of approximately 1.2 mm was obtained at a treatment time of 6 min. Hence there was only a slight increase of about 0.2 mm for a treatment time of 6 min. In lateral direction the maximum value for the SD of the marker positions was 1.8 mm. In longitudinal direction the initial average SD of the markers' position resulted in about 1.1 mm (see Fig. 4.15(b)). It showed a steeper increase compared to lateral direction to about 1.8 mm at a treatment time of 6 min. The peak value for the SD of the prostate's position after treatment delivery was about 2.5 mm. The initial average SD of the markers' position in vertical direction resulted in a value of approximately 1 mm (see Fig. 4.15(c)). The trend line in vertical direction showed an increase with treatment time to about 1.7 mm at a time of 6 min. A maximum value of 2.3 mm was obtained for the SD of the markers' position in vertical direction for a patient after 4-field box irradiation delivery.

4.3 Overview of Uncertainties

The mean systematic error, M, the SD of the systematic error, Σ, and the SD of the random error, σ, for bone intrafraction motion at the end of a treatment fraction are shown in table 4.2 for 5-field boost IMRT, 9-field pelvic IMRT and 4-field box treatments. To obtain the net whole-patient movement the initial position of the bony anatomy was defined as 0, 0, 0 in lateral, longitudinal and vertical direction, respectively.

Table 4.3 shows the mean systematic error, M, the SD of the systematic error, Σ, and the SD of the random error, σ, after daily fractions for prostate intrafraction motion for 5-field boost IMRT, 9-field pelvic IMRT and 4-field box treatments. The markers' position obtained through

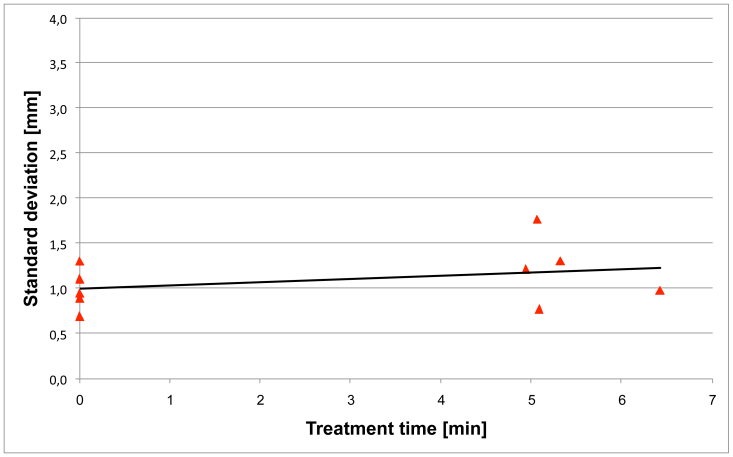

(a) lateral direction

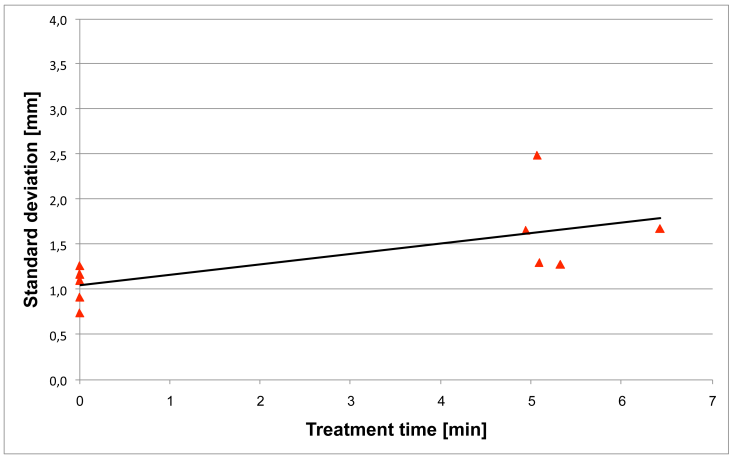

(b) longitudinal direction

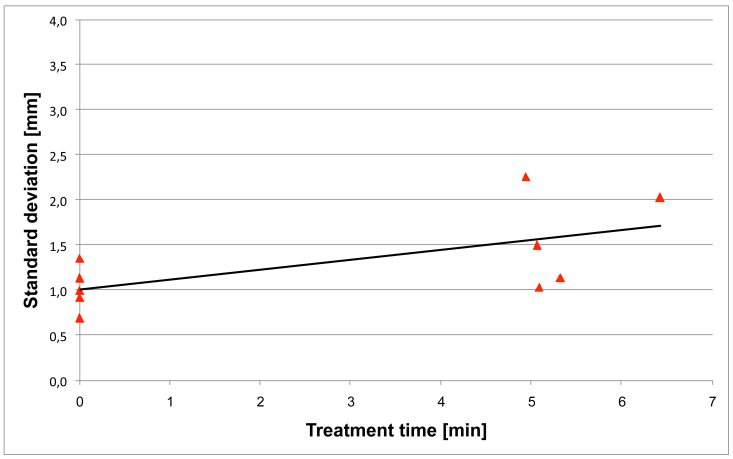

(c) vertical direction

Figure 4.15: Standard deviations of marker positions for each 4-field box patient before and after treatment delivery.

Table 4.3: Marker intrafraction motion (corrected for whole-patient movement and setup tolerance): group systematic error, M, standard deviation of the systematic error, Σ, and standard deviation of the random error, σ, for 5-field boost IMRT, 9-field pelvic IMRT and 4-field box treatments in lateral, longitudinal and vertical direction, respectively.

	5-field IMRT			9-field IMRT			4-field box		
[mm]	lat	long	vert	lat	long	vert	lat	long	vert
M	0.1	0.0	0.1	0.0	-0.5	-0.2	-0.1	0.4	0.1
Σ	0.2	0.5	0.7	0.2	1.2	1.3	0.1	0.6	0.5
σ	0.5	1.1	1.5	0.7	1.7	1.9	0.7	1.5	1.2

Table 4.4: Marker displacement after treatment fraction: group systematic error, M, standard deviation of the systematic error, Σ, and standard deviation of the random error, σ, for 5-field boost IMRT, 9-field pelvic IMRT and 4-field box treatments in lateral, longitudinal and vertical direction, respectively.

	5-field IMRT			9-field IMRT			4-field box		
[mm]	lat	long	vert	lat	long	vert	lat	long	vert
M	0.1	0.2	-0.9	0.4	-0.4	-1.6	0.4	0.9	-0.2
Σ	1.0	0.6	0.9	1.3	1.5	2.0	0.4	1.1	1.2
σ	1.7	1.5	2.0	1.4	1.9	2.3	1.8	1.8	1.9

the ExacTrac system was corrected for setup tolerance and whole-patient motion to obtain the net intrafraction motion of the prostate.

The mean systematic error, M, the SD of the systematic error, Σ, and the SD of the random error, σ, after a daily treatment fraction are shown for the gross prostate displacement in table 4.4 for 5-field boost IMRT, 9-field pelvic IMRT and 4-field box treatments. The impact of whole-patient movement and setup tolerance to the positioning error after the delivery of a fraction is already included in the calculated data.

4.4 Implications for Margins

Margins accounting for intrafraction prostate and patient motion as well as for uncertainties caused through the 3 mm setup tolerance were calculated according to van Herk's formula (Equ. 2.17) for 5-field boost IMRT, 9-field pelvic IMRT and 4-field box treatments based on the data from table 4.4, respectively. For 9-field pelvic IMRT and 4-field box treatments the margins are smallest in lateral direction and largest in vertical direction. In contrast, for 5-field

Table 4.5: Margins accounting for intrafraction motion and setup tolerance.

	Margins [mm]			Mean treatment	No. of evaluated
	lat	long	vert	time [min]	fractions
5-field IMRT	3.7	2.6	3.6	9.7 (7.6-12.2)	96
9-field IMRT	4.2	5.1	6.6	16.2 (14.3-18.0)	317
4-field box	2.2	3.9	4.3	5.4 (4.9-6.4)	174
currently used	10	10	10/5		

Table 4.6: Contributions to margins for IMRT and 4-field box treatments.

	Margins [mm]		
	lat	long	vert
5-field IMRT	3.7	2.6	3.6
setup error	1.5	1.8	2.0
bone motion	2.7	1.1	1.3
marker motion	0.9	2.0	2.9
9-field IMRT	4.2	5.1	6.6
setup error	1.8	1.5	2.2
bone motion	3.0	1.1	3.6
marker motion	1.1	4.3	4.5
4-field box	2.2	3.9	4.3
setup error	1.2	1.7	2.2
bone motion	1.4	0.9	1.0
marker motion	0.8	2.6	2.1

boost IMRT the obtained margins are largest in lateral direction and smallest in longitudinal direction, but show only differences in the order of one to two milimeters (see Tab. 4.5). To evaluate this issue margins calculated for the single net contributions to the overall prostate's location uncertainty, which are **setup error**, **net bone motion** and **net prostate movement**, are shown in table 4.6.

4.5 Endorectal Balloon

The day-to-day variation of the balloon's position after insertion was qualitatively analysed for 4 patients. Therefore, the ERB was delineated in the planning CT, which enabled a matching according to the balloon's position with the ExacTrac system. The position of the balloon was determined relative to bony anatomy at the begin of a fraction. Hence for as far as possible each

fraction the displacement of the balloon relative to its position in the planning CT (evaluation of the difference between bone match and balloon match) is shown in Fig. 4.16 for lateral, longitudinal and vertical direction, respectively. The evaluation started with the patient represented through the dark blue dots in treatment fraction number 6. Unfortunately the patient could not bear the balloon anymore after fraction number 10 and therefore was treated without an ERB for the remaining fractions. For the other 3 patients the examination started with the begin of the radiotherapy treatment series, although the line for the patients depicted by the light green diamonds and the pale blue squares shows a gap due to maintenance activities at the linac, where the patients were treated at another device without ExacTrac system. The displacement of the balloon was in general smallest in lateral direction, with a maximum displacement of 8 mm (see Fig. 4.16(a)). In longitudinal and vertical direction, where the displacement of the balloon was much larger than in lateral direction it can be seen that it was strongly patient dependent. For the patient symbolized through the light green diamonds the displacement was remarkably large in longitudinal direction and the balloon was at the maximum 25 mm too much caudal (see Fig. 4.16(b)). The balloon was generally placed too much caudal for all patients. Having a closer look at the whole patient population evaluated for balloon displacement, the balloon displacement in vertical direction was in general smaller than for longitudinal direction (see Fig. 4.16(c)). However, again for the patient represented by the light green diamonds quite large values of displacement up to 18 mm were reached. Generally, the balloon was positioned too much posterior.

The calculated mean systematic displacement, M, the SD of the systematic displacement, Σ, and the SD of the random displacement, σ, can be found in table 4.7 for lateral, longitudinal and vertical direction, respectively. Though, this data is only presented to express trends, due to the fact that the amount of data is not sufficient to allow a quantitative analysis.

Having a look at the 3D displacement of the endorectal balloon calculated from the values of displacement in lateral, longitudinal and vertical direction, it manifests that the balloon's position in the planning CT is not reproducible (see Fig. 4.17), as 3D deviations of up to 28 mm occur.

Additionally, differences in the volume of the endorectal balloon were observed when matching the radiographic images according to the balloon's position, which could not be quantitatively evaluated. One has to keep in mind this extra source of uncertainty, when investigating the reproducibility of the balloon's position and its capability for immobilization of the prostate.

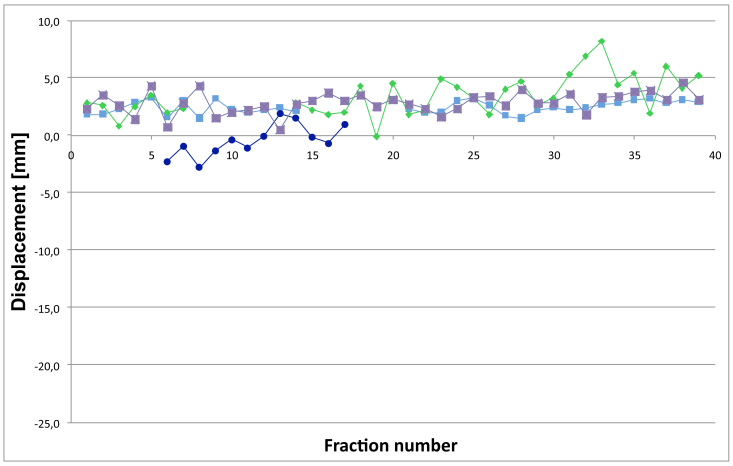

(a) lateral direction

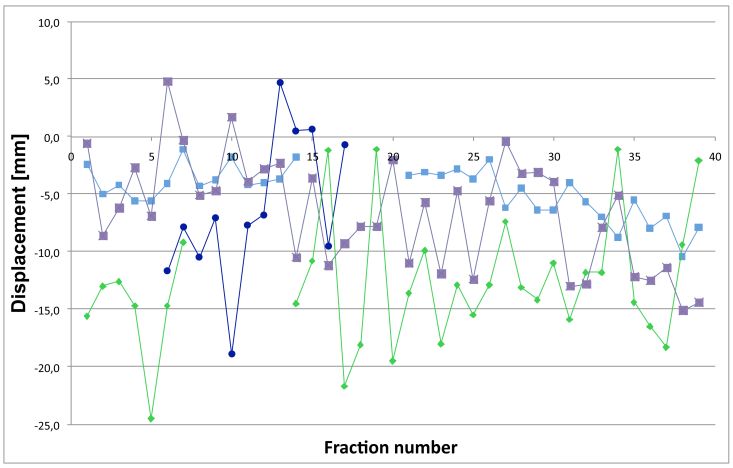

(b) longitudinal direction

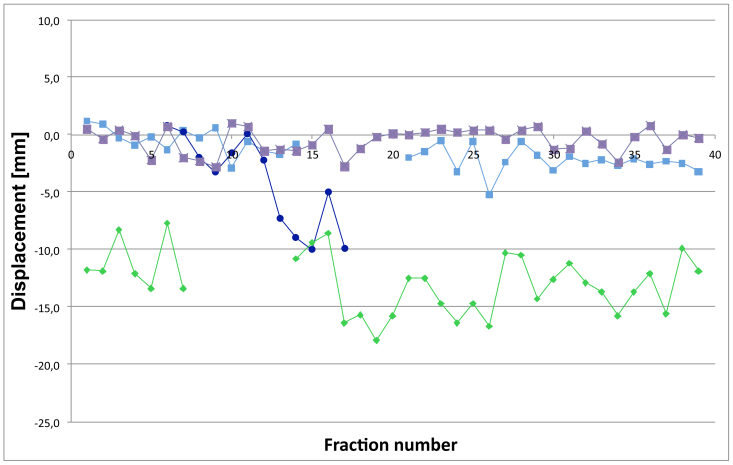

(c) vertical direction

Figure 4.16: Displacement of endorectal balloon after insertion in relation to its position in the planning CT for daily fractions and several patients (color = patient).

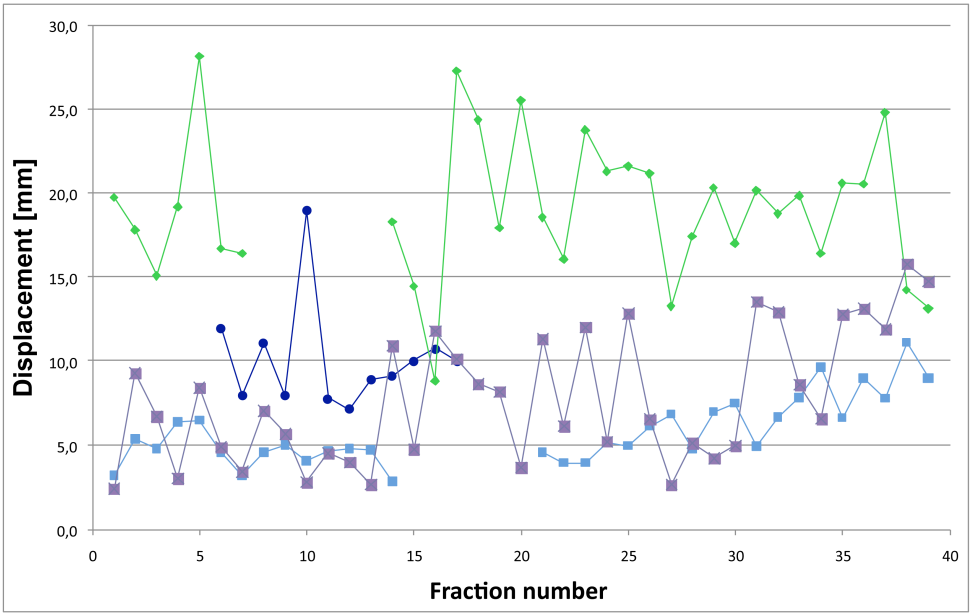

Figure 4.17: 3D displacement of endorectal balloon after insertion in relation to its position in the planning CT for daily fractions and several patients (color = patient).

Table 4.7: Balloon displacement relative to its position in the planning CT with respect to bony anatomy: group systematic error, M, standard deviation of the systematic error, Σ, and standard deviation of the random error, σ, in lateral, longitudinal and vertical direction, respectively.

$[mm]$	lat	long	vert
M	2.1	-7.6	-4.7
Σ	1.5	3.1	4.9
σ	1.2	4.9	2.5

4.6 Rotations of the Target Volume

As the ExacTrac system provided only a limited ability to state the rotations of the target volume (depending on the particular patient, from 5 % to 97 % of all treatment fractions) and the utilized treatment couch did not offer the opportunity for rotational corrections, rotations of the target volume were not further investigated.

The mean rotations for all IMRT patients after setup correction right before irradiation start were 1.4°, 0.9° and 0.1° around the lateral, longitudinal and vertical axis, respectively. The extreme values were about 10° and -9° around both, the lateral and longitudinal axis and about ±4° around the vertical axis.

5 Discussion

5.1 Intrafraction Motion and Margins

As seen in Fig. 4.1 and Fig. 4.3(a) the magnitude of intrafractional patient motion is strongly patient dependent. Though, the patient represented through red triangular symbols is especially outstanding due to larger movements compared to all other patients. Looking for a reason for this behaviour the quite remarkable BMI of 37.9 is noticeable. However, having a closer look at the displacement of bony anatomy and prostate itself for all other patients with a high BMI, no obvious trends could be observed. Thus for correlating large whole-body movement or prostate displacement to high values for BMI there is not enough evidence in the obtained data.

Whole-patient motion was in general smallest in longitudinal direction, which can also be seen in the net bone motion contribution to the treatment margin (see Tab. 4.6). This may be explained through the fact that a knee support was used for patient immobilization, which seemed to prevent the patients from moving easily in cranial-caudal direction. Surveying the SDs for the bone drifts, on average the largest bone movement occurred in lateral direction (see Fig. 4.4(a)). A peak value of 3.1 mm for the SD of bone motion in lateral direction after treatment delivery was obtained for a patient receiving a 5-field boost treatment. This fact seems to be surprising at first glance, as the average irradiation time of 9.7 min for the boost fractions is much shorter than the mean treatment time of 16.2 min for the 9-field pelvic IMRT fractions, and the SD of bone movement generally increased as a function of treatment time. However, receiving large values for the SD of bone motion for boost fractions could be explained through the fact that the boost treatments are the first 11 fractions in the treatment course and particular patients might be more nervous during the first fractions and therefore moving more than for later fractions. The outstanding large SDs in vertical direction of 2.9 mm and 3.6 mm (see Fig. 4.4(c)) were obtained for the patient depicted by red triangular symbols in Fig. 4.1 during and after 9-field pelvic IMRT fraction delivery, respectively.

In contrast to the motion of bony anatomy, prostate movement was less dependent on patients (see Fig. 4.2 and Fig. 4.3(b)). The marker displacement showed a significant increase with treatment time in longitudinal and vertical direction, while the prostate stayed rather stable in lateral direction. The prostate's stability concerning motion in lateral direction was also reported by Both et al. [41]. The contributions for the net prostate motion to the treatment margin for

lateral, longitudinal and vertical direction support this conclusion (see Tab. 4.6). As one can see from Fig. 4.2(b) for the longitudinal direction of prostate motion, the prostate seemed to move slightly caudal during a treatment fraction. This could be explained through the fact that the bladder might fill up during longer (for 9-field pelvic IMRT fractions the mean net treatment time was 16.2 min) treatment fractions and apply pressure to the prostate, which is accordingly moving caudal (see Fig. 2.15). Also, the prostate seemed to move a little posterior for longer treatment times. Thus a posterior motion of the prostate could be correlated to a caudal motion as well and might occur because of the same reason, i. e. the bladder is filled during a treatment fraction. Lotz et al. reported an inflow rate of 2.1 to 15 cc/min for patients, who were told to empty their bladder and then drink 300 cc water 15 min prior to MRI acquisition, which took one hour [43].

As seen in Tab. 4.5, the calculated margins are smallest in lateral direction (4.2 mm and 2.2 mm) and largest in vertical direction (6.6 mm and 4.3 mm) for 9-field pelvic IMRT and 4-field box treatments, respectively. For 5-field boost IMRT, however, the largest value was obtained in lateral direction (3.7 mm) and the smallest value in longitudinal direction (2.6 mm). To address this issue, it is necessary to have a closer look at the margins calculated for the single net contributions to the overall prostate's location uncertainty (see Tab. 4.6). It is apparent that the margins calculated for the setup error do not differ a lot for each direction of 5-field IMRT, 9-field-IMRT and 4-field box treatments and always are largest in vertical direction. This result was also presented by Graf et al. [31]. The reason could be a possible relaxation of the pelvic floor muscles. Budiharto et al. evaluated the residual setup error by use of an online MV imager and concluded that a systematic setup error in posterior direction after the repositioning of the patient occurred [44]. For 5-field boost IMRT and 9-field pelvic IMRT the component accounting for net prostate motion always is smallest in lateral direction and largest in vertical direction. Again, the smallest values were measured in lateral direction for 4-field box treatments. However, for 4-field box treatments the largest value for the net prostate motion was obtained for longitudinal direction. This could be explained due to the small population of 5 patients evaluated for 4-field box treatments. Margins calculated for net bone motion during a fraction are in general smallest in longitudinal direction. For 5-field IMRT and 4-field box treatments the largest values for bone motion were obtained in lateral direction. The margin accounting for the net whole-patient movement was largest in vertical direction for the 9-field IMRT, where the values for lateral and vertical direction exceeded the value for

longitudinal direction quite remarkably. This is caused through large SDs of the systematic error (see Tab. 4.2), which might be a result of the inclusion of patients, who moved quite extensively during treatment delivery. For the 9-field pelvic IMRT the trend for the net prostate motion concerning the magnitude of the margins for lateral, longitudinal and vertical direction concealed the trend for net whole-patient movement. For the 5-field boost IMRT the component accounting for bone motion was more dominant in comparison to marker displacement and therefore the trend indicated by the net prostate motion was overshot through net bone motion. This could be explained through the fact that the boost fractions were scheduled as the first 11 fractions of the treatment series and the patients were more nervous and uneasy than for the later 9-field pelvic IMRT fractions. For 4-field box treatments the data of all 39 fractions was summed up, therefore, a possibly larger initial bone motion had lower impact than for the 5-field boost IMRT.

When calculating margins for treatment one has to keep in mind that the acquired images just represent snapshots, which give an estimation for long-term intrafraction motion. Short-term variations of the prostate's position cannot be traced using this method [28, 30, 42]. However, Both et al. used a real-time tracking system and reported that the use of an endorectal balloon stabilizes large (> 5 mm) prostate movement, as it prevents the influence of bowel habit changes [41].

Another issue is that for 9-field pelvic IMRTs the PTV consists of the prostate and the PLNs, with the prostate being a moving target with respect to bony anatomy and the PLNs being fixed to vascular structures, which are again fixed to bony anatomy. Hence the intrafraction motion of the prostate can be described through the motion of the fiducial markers, while for the movement of the PLNs the motion of bony anatomy might be a better approximation. For concurrent irradiation of prostate and PLNs Xia et al. suggested real time replanning, or the creation of several IMRT plans for different positions of the prostate to tackle the challenge of independent motion [28, 45].

Also, one has to consider, that the obtained margins (see Tab. 4.5) do not account for other sources of uncertainty (like inter- and intraobserver variability in target volume delineation), which have to be dealt with.

5.2 Comparison with Literature

Intrafraction prostate and patient motion causes significant positioning variations, which have to be accounted for by use of appropriate margins. The margins calculated based on the

Table 5.1: Comparison of obtained margins for IMRT patients with results from literature.

Author	No. of fields	PTV	Setup tolerance [mm]	Margins [mm] lat	long	vert	Treatment time [min]	No. of patients
This study	5	P	3	3.7	2.6	3.6	9.7	9
	9	P+PLN	3	4.2	5.1	6.6	16.2	12
Enmark et al. [27]	5-7	P+SV	2	1.9	2.6	2.4	9.0	15
Alonso-Arr. et al. [28]	7	-	2	1.9	6.2	4.7	-	30
Kron et al. [30]	-	-	0	1.9	2.8	3.0	6-9	184
	-	-	0	3.1	4.0	4.0	>9	184
Tanyi et al. [46]	7	P	3	2.8	3.7	3.2	8-16	14

data acquired in this study were comparable to results from literature where no endorectal balloon was used (see Tab. 5.1). Enmark et al. [27] evaluated the intrafraction prostate motion by use of 3 fiducial markers within the prostate and image acquisition pre and post treatment with the ExacTrac system. Alonso-Arrizabalaga et al. [28] examined intrafraction prostate motion by imaging with the ExacTrac system before and after treatment for patients with 4 fiducial markers inside the prostate. Kron et al. [30] investigated the data of 184 patients with 3 inserted fiducial markers through imaging pre and post treatment delivery by use of two orthogonal X-ray projections, forming groups in terms of treatment duration (see Tab. 5.1). At least one image per patient was included to both groups with treatment lengths of 6-9 min and > 9 min. Tanyi et al. [46] evaluated margins necessary to deal with intrafraction prostate motion using 3 electromagnetic transponders implanted within the prostate. For real-time tracking using the Calypso® system they obtained margins of 1.4 mm, 2.6 mm and 2.3 mm for lateral, longitudinal and vertical direction, respectively, when applying a threshold for corrective intervention for a displacement of 4 mm lasting longer than 1 s. Assuming just an initial image-guided alignment of the target volume, considering intrafraction motion, Tanyi et al. stated margins of 2.8 mm, 3.7 mm and 3.2 mm for lateral, longitudinal and vertical direction, respectively, indicated in the last line of Tab. 5.1.

As the setup tolerance at the Medical University of Vienna/AKH was larger than for most other studies, a reduction should be considered to decrease the component of setup error contributing to the overall margin for treatment.

5.3 Endorectal Balloon

According to the data presented in Fig. 4.16 and Fig. 4.17 the daily position of the ERB is not reproducible. The largest variations of the balloon's position occurred in longitudinal direction. A reason might be that various RTTs tend to place the ERB at different depths. The balloon was in general positioned too much posterior and too much caudal, inducing the assumption that there is a correlation between these displacements. An ERB with depth markers, as Smeenk et al. reported, might be beneficial to avoid large deviations of the balloon's position in longitudinal direction [40, 47]. However, comparing the obtained margins to results from literature where no ERB was used, they are in the same order of magnitude. As Anderson et al. reported a significant decrease in rectal volume over the radiotherapy treatment course of prostate cancer [48] the use of an ERB would by all means be beneficial in terms of rectal wall sparing through keeping the posterior rectal wall away from the target volume.

Further investigations will be necessary to evaluate whether the insufficient reproducibility of the balloon's position is an issue concerning its ability for immobilization of the prostate. Van Lin et al. [49] indicated that an ERB does not reduce interfraction prostate motion. Concerning intrafraction prostate motion Both et al. [41] reported an advantage in terms of magnitude of the applicable margins when using a daily ERB in comparison to Langen et al. [33], who evaluated a non-ERB setup, as the percentage of treatment time where the displacement exceeded certain values was reduced through utilization of an ERB. As in this study the evaluation of the balloon's position was performed for a patient population different from the patients, where intrafraction prostate and whole-patient motion were investigated, a correlation of a balloon shift and a prostate shift is impossible at this point, but would be interesting to be further explored. Also, changes in filling volume of the balloon were observed, when fusing the daily ExacTrac images with the reconstructed images from planning CT. Though, these issues could not be evaluated through the ExacTrac system. A change in size of the balloon might have an impact on the position where the prostate is stabilized and should therefore be further investigated. Another issue is a possible prostate shift as a result of muscle relaxation after insertion of the ERB, as Court et al. considered. Hence he suggested to wait for relaxation before starting irradiation to avoid a target movement while treatment was delivered [50].

6 Conclusion

Intrafraction prostate motion showed a significant increase with treatment time in longitudinal and vertical direction for all patients. In lateral direction the prostate stayed rather stable. In contrast, intrafraction patient movement was strongly patient dependent and, in general, smallest for longitudinal direction. Also, bone displacement increased as a function of treatment time. Hence significant positioning errors caused through intrafraction prostate and patient motion have to be accounted for by application of appropriate margins related to the time duration of daily irradiation delivery.

Complex treatments like the 9-field pelvic IMRT with long treatment times of about 16 min accordingly require larger margins compared to shorter treatment times (see Tab. 4.5) to assure target coverage for the duration of the whole fraction. Thus when aiming to further reduce the treatment margin, additional imaging and repositioning of the patients during the treatment will be necessary. However, this is causing a controversy as the procedure would again increase the gross treatment time and the patients might become uneasier. Therefore, other approaches are the utilization of new treatment techniques like rotational IMRT, which offers the advantage of shorter treatment fractions (< 1.5 min) [51], electromagnetic real-time tracking [41, 52, 53], requiring additional equipment, and adaptive radiotherapy, where the treatment plan for a patient is modified for later fractions after collecting information concerning the magnitude of intrafraction motion during the initial fractions [54].

The use of an ERB seems to be beneficial in terms of sparing the rectal wall. According to the data obtained in this study the calculated margins accounting for intrafraction target motion are of the same magnitude as for other studies where no ERB was utilized. There are still issues concerning the ability of the ERB for prostate immobilization, as well as the reproducibility of its daily position and volume, which require further investigations.

Bibliography

[1] H. Dieter Kogelnik. Inauguration of radiotherapy as a new scientific speciality by Leopold Freund 100 years ago. *Radiotherapy and Oncology*, 42(3):203–211, 1997.

[2] P. H. Cossmann. *Medizintechnik*, chapter Medizinische Strahlentherapie, pages 539–555. Springer Medizin Verlag Heidelberg, 3rd edition, 2007.

[3] Hanno Krieger. *Grundlagen der Strahlungsphysik und des Strahlenschutzes.* Vieweg+Teubner GWV Fachverlage GmbH, Wiesbaden, 3rd edition, 2009.

[4] Murat Beyzadeoglu, Gokhan Ozyigit, and Cuneyt Ebruli. *Basic Radiation Oncology.* Spinger-Verlag Berlin Heidelberg, 2010.

[5] Faiz M. Khan. *The Physics of Radiation Therapy.* Lippincott Williams & Wilkins, 3rd edition, 2003.

[6] P. Mayles, A. Nahum, and J. C. Rosenwald, editors. *Handbook of radiotherapy physics: theory and practice.* Taylor & Francis Group, LLC, 2007.

[7] Michael Wannenmacher, Jürgen Debus, and Frederik Wenz, editors. *Strahlentherapie.* Springer Berlin / Heidelberg, 2006.

[8] E. B. Podgorsak, editor. *Radiation oncology physics : a handbook for teachers and students.* IAEA, 2005.

[9] Gabriele Kragl, Sacha af Wetterstedt, Barbara Knäusl, Mårten Lind, Patrick McCavana, Tommy Knöös, Brendan McClean, and Dietmar Georg. Dosimetric characteristics of 6 and 10 MV unflattened photon beams. *Radiotherapy and Oncology*, 93(1):141–146, 2009.

[10] Laura A. Dawson and Cynthia Ménard. Imaging in radiation oncology: A perspective. *The Oncologist*, 15(4):338–349, 2010.

[11] Neil G. Burnet, Simon J. Thomas, Kate E. Burton, and Sarah J. Jefferies. Defining the tumour and target volumes for radiotherapy. *Cancer Imaging*, 4(2):153–161, 2004.

[12] ICRU. ICRU Report 50: Prescribing, Recording, and Reporting Photon Beam Therapy. Technical report, International Commission on Radiation Units and Measurements, Bethesda, Maryland, September 1993.

[13] ICRU. ICRU Report 83: Prescribing, Recording, and Reporting Photon-Beam Intensity-Modulated Radiation Therapy (IMRT). *Journal of the ICRU*, 10(1):1–106, April 2010.

[14] S. A. Bhide and C. M. Nutting. Recent advances in radiotherapy. *BMC Medicine*, 8(1):25, 2010.

[15] David Palma, Emily Vollans, Kerry James, Sandy Nakano, Vitali Moiseenko, Richard Shaffer, Michael McKenzie, James Morris, and Karl Otto. Volumetric modulated arc therapy for delivery of prostate radiotherapy: Comparison with intensity-modulated radiotherapy and three-dimensional conformal radiotherapy. *International Journal of Radiation Oncology*Biology*Physics*, 72(4):996–1001, 2008.

[16] Spiridon V. Spirou and Chen S. Chui. Generation of arbitrary intensity profiles by dynamic jaws or multileaf collimators. *Medical Physics*, 21(7):1031–1041, 1994.

[17] U. Oelfke and T. Bortfeld. Inverse planning for photon and proton beams. *Medical Dosimetry*, 26(2):113–124, 2001.

[18] Dirk Verellen, Mark De Ridder, and Guy Storme. A (short) history of image-guided radiotherapy. *Radiotherapy and Oncology*, 86(1):4–13, 2008.

[19] AAPM Task Group 104. The role of in-room kV X-ray imaging for patient setup and target localization. Technical report, American Association of Physicists in Medicine, 2009.

[20] Marcel van Herk. Errors and margins in radiotherapy. *Seminars in Radiation Oncology*, 14(1):52–64, 2004.

[21] Marcel van Herk, Peter Remeijer, Coen Rasch, and Joos V. Lebesque. The probability of correct target dosage: dose-population histograms for deriving treatment margins in radiotherapy. *International Journal of Radiation Oncology*Biology*Physics*, 47(4):1121–1135, 2000.

[22] Ahmedin Jemal, Freddie Bray, Melissa M. Center, Jacques Ferlay, Elizabeth Ward, and David Forman. Global cancer statistics. *CA: A Cancer Journal for Clinicians*, 61(2):69–90, 2011.

[23] Ernst Mutschler, Hans-Georg Schaible, and Peter Vaupel. *Anatomie Physiologie Pathophysiologie des Menschen.* Wissenschaftliche Verlagsgesellschaft mbH Stuttgart, 6th edition, 2007.

[24] L. H. Sobin, M. K. Gospodarowicz, and Ch. Wittekind, editors. *TNM Classification of Malignant Tumours*. Wiley-Blackwell, Chichester, West Sussex, UK, 2010.

[25] Thomas M. Pisansky. External beam radiotherapy as curative treatment of prostate cancer. *Mayo Clinic Proceedings*, 80(7):883–898, 2005.

[26] Dirk Boehmer, Philippe Maingon, Philip Poortmans, Marie-Hélène Baron, Raymond Miralbell, Vincent Remouchamps, Christopher Scrase, Alberto Bossi, and Michel Bolla. Guidelines for primary radiotherapy of patients with prostate cancer. *Radiotherapy and Oncology*, 79(3):259–269, 2006.

[27] Marika Enmark, Stine Korreman, and Håkan Nyström. IGRT of prostate cancer; is the margin reduction gained from daily IG time-dependent? *Acta Oncologica*, 45(7):907–914, 2006.

[28] Sara Alonso-Arrizabalaga, Luis Brualla González, Juan V. Roselló Ferrando, Jorge Pastor Peidro, José López Torrecilla, Domingo Planes Meseguer, and Trinidad García Hernández. Prostate planning treatment volume margin calculation based on the ExacTrac X-ray 6D image-guided system: Margins for various clinical implementations. *International Journal of Radiation Oncology*Biology*Physics*, 69(3):936–943, 2007.

[29] Maaike R. Moman, Uulke A. van der Heide, Alexis N.T.J. Kotte, R. Jeroen A. van Moorselaar, Gijsbert H. Bol, Stefan P.G. Franken, and Marco van Vulpen. Long-term experience with transrectal and transperineal implantations of fiducial gold markers in the prostate for position verification in external beam radiotherapy; feasibility, toxicity and quality of life. *Radiotherapy and Oncology*, 96(1):38–42, 2010.

[30] Tomas Kron, Jessica Thomas, Chris Fox, Ann Thompson, Rebecca Owen, Alan Herschtal, Annette Haworth, Keen-Hun Tai, and Farshad Foroudi. Intra-fraction prostate displacement in radiotherapy estimated from pre- and post-treatment imaging of patients with implanted fiducial markers. *Radiotherapy and Oncology*, 95(2):191–197, 2010.

[31] Reinhold Graf, Dirk Boehmer, Volker Budach, and Peter Wust. Residual translational and rotational errors after kV X-ray image-guided correction of prostate location using implanted fiducials. *Strahlentherapie und Onkologie*, 186:544–550, 2010.

[32] Brandon M. Barney, R. Jeffrey Lee, Diana Handrahan, Keith T. Welsh, J. Taylor Cook, and William T. Sause. Image-guided radiotherapy (IGRT) for prostate cancer comparing kV

imaging of fiducial markers with cone beam computed tomography (CBCT). *International Journal of Radiation Oncology*Biology*Physics*, 80(1):301–305, 2011.

[33] Katja M. Langen, Twyla R. Willoughby, Sanford L. Meeks, Anand Santhanam, Alexis Cunningham, Lisa Levine, and Patrick A. Kupelian. Observations on real-time prostate gland motion using electromagnetic tracking. *International Journal of Radiation Oncology*Biology*Physics*, 71(4):1084–1090, 2008.

[34] Julian Perks, Helen Turnbull, Tianxiao Liu, James Purdy, and Richard Valicenti. Vector analysis of prostate patient setup with image-guided radiation therapy via kV cone beam computed tomography. *International Journal of Radiation Oncology*Biology*Physics*, 79(3):915–919, 2011.

[35] Cornelia Walter, Judit Boda-Heggemann, Hansjörg Wertz, Iris Loeb, Angelika Rahn, Frank Lohr, and Frederik Wenz. Phantom and in-vivo measurements of dose exposure by image-guided radiotherapy (IGRT): MV portal images vs. kV portal images vs. cone-beam CT. *Radiotherapy and Oncology*, 85(3):418–423, December 2007.

[36] Guy Soete, Dirk Verellen, Dirk Michielsen, Vincent Vinh-Hung, Jan Van de Steene, Dirk Van den Berge, Patricia De Roover, Frans Keuppens, and Guy Storme. Clinical use of stereoscopic X-ray positioning of patients treated with conformal radiotherapy for prostate cancers. *International Journal of Radiation Oncology*Biology*Physics*, 54(3):948–952, 2002.

[37] Áshildur Logadóttir, Stine Korreman, and Peter Meidahl Petersen. Comparison of the accuracy and precision of prostate localization with 2D-2D and 3D images. *Radiotherapy and Oncology*, 98(2):175–180, 2011.

[38] BrainLAB AG, Heimstetten - Deutschland. *Klinisches Handbuch Novalis Body / ExacTrac*, 5.0 edition, 2006.

[39] Mack Roach III, Michelle DeSilvio, Richard Valicenti, David Grignon, Sucha O. Asbell, Colleen Lawton, Charles R. Thomas, Jr., and William U. Shipley. Whole-pelvis, "mini-pelvis," or prostate-only external beam radiotherapy after neoadjuvant and concurrent hormonal therapy in patients treated in the Radiation Therapy Oncology Group 9413 trial. *International Journal of Radiation Oncology*Biology*Physics*, 66(3):647–653, 2006.

[40] Robert Jan Smeenk, Bin S. Teh, E. Brian Butler, Emile N.J.Th. van Lin, and Johannes H.A.M. Kaanders. Is there a role for endorectal balloons in prostate radiotherapy? A systematic review. *Radiotherapy and Oncology*, 95(3):277–282, 2010.

[41] Stefan Both, Ken Kang-Hsin Wang, John P. Plastaras, Curtiland Deville, Voika Bar Ad, Zelig Tochner, and Neha Vapiwala. Real-time study of prostate intrafraction motion during external beam radiotherapy with daily endorectal balloon. *International Journal of Radiation Oncology*Biology*Physics*, In Press, Corrected Proof:–, 2010.

[42] Eugene Huang, Lei Dong, Anurag Chandra, Deborah A. Kuban, Isaac I. Rosen, Anissa Evans, and Alan Pollack. Intrafraction prostate motion during IMRT for prostate cancers. *International Journal of Radiation Oncology*Biology*Physics*, 53(2):261–268, 2002.

[43] Heidi T. Lotz, Marcel van Herk, Anja Betgen, Floris Pos, Joos V. Lebesque, and Peter Remeijer. Reproducibility of the bladder shape and bladder shape changes during filling. *Medical Physics*, 32(8):2590–2597, 2005.

[44] Tom Budiharto, Pieter Slagmolen, Karin Haustermans, Frederik Maes, Sara Junius, Jan Verstraete, Raymond Oyen, Jeroen Hermans, and Frank Van den Heuvel. Intrafractional prostate motion during online image guided intensity-modulated radiotherapy for prostate cancer. *Radiotherapy and Oncology*, 98(2):181–186, 2011.

[45] Ping Xia, Peng Qi, Andrew Hwang, Erica Kinsey, Jean Pouliot, and Mack III Roach. Comparison of three strategies in management of independent movement of the prostate and pelvic lymph nodes. *Medical Physics*, 37(9):5006–5013, 2010.

[46] James A. Tanyi, Tongming He, Paige A. Summers, Ruth G. Mburu, Catherine M. Kato, Stephen M. Rhodes, Arthur Y. Hung, and Martin Fuss. Assessment of planning target volume margins for intensity-modulated radiotherapy of the prostate gland: Role of daily inter- and intrafraction motion. *International Journal of Radiation Oncology*Biology*Physics*, 78(5):1579–1585, 2010.

[47] Robert Jan Smeenk, Emile N.J.Th. van Lin, Peter van Kollenburg, Martina Kunze-Busch, and Johannes H.A.M. Kaanders. Anal wall sparing effect of an endorectal balloon in 3D conformal and intensity-modulated prostate radiotherapy. *Radiotherapy and Oncology*, 93(1):131–136, 2009.

[48] Nicole S. Anderson, James B. Yu, Richard E. Peschel, and Roy H. Decker. A significant decrease in rectal volume and diameter during prostate IMRT. *Radiotherapy and Oncology*, 98(2):187–191, 2011.

[49] Emile N.J. Th. van Lin, Lisette P. van der Vight, J. Alfred Witjes, HenkJan J. Huisman, Jan Willem Leer, and Andries G. Visser. The effect of an endorectal balloon and off-line correction on the interfraction systematic and random prostate position variations: A comparative study. *International Journal of Radiation Oncology*Biology*Physics*, 61(1):278–288, 2005.

[50] Laurence E. Court, Anthony V. D'Amico, Dnyanesh Kadam, and Robert Cormack. Motion and shape change when using an endorectal balloon during prostate radiation therapy. *Radiotherapy and Oncology*, 81(2):184–189, 2006.

[51] Marianne C. Aznar, Peter Meidahl Petersen, Ashildur Logadottir, Henriette Lindberg, Stine S. Korreman, Flemming Kjær-Kristoffersen, and Svend Aage Engelholm. Rotational radiotherapy for prostate cancer in clinical practice. *Radiotherapy and Oncology*, 97(3):480–484, December 2010.

[52] Zhong Su, Lisha Zhang, Martin Murphy, and Jeffrey Williamson. Analysis of prostate patient setup and tracking data: Potential intervention strategies. *International Journal of Radiation Oncology*Biology*Physics*, In Press, Corrected Proof:–, 2010.

[53] Shinichi Shimizu, Yasuhiro Osaka, Nobuo Shinohara, Ataru Sazawa, Kentaro Nishioka, Ryusuke Suzuki, Rikiya Onimaru, and Hiroki Shirato. Use of implanted markers and interportal adjustment with real-time tracking radiotherapy system to reduce intrafraction prostate motion. *International Journal of Radiation Oncology*Biology*Physics*, In Press, Corrected Proof:–, 2011.

[54] Justus Adamson and Qiuwen Wu. Prostate intrafraction motion assessed by simultaneous kV fluoroscopy at MV delivery II: Adaptive strategies. *International Journal of Radiation Oncology*Biology*Physics*, 78(5):1323–1330, 2010.

List of Figures

List of Tables